

國立交通大學
電子物理研究所

碩士論文

具平面式與嵌入式電極
氮化鎵金屬-半導體-金屬光偵測器之
製程與光電特性

Process and Optoelectronic Characterization of Planar and Recessed
Electrodes GaN Metal-Semiconductor-Metal Photodetectors

研究生：蔡東昇

指導教授：楊賜麟 博士

中華民國九十四年七月

具平面式與嵌入式電極之氮化鎵金屬-半導體-金屬光偵測器

之製程與光電特性

Process and Optoelectronic Characterization of Planar and Recessed Electrodes
GaN Metal-Semiconductor-Metal Photodetector

研究生：蔡東昇

Student : Dung-Sheng Tsai

指導教授：楊賜麟 博士

Advisor : Dr. Su-Lin Yang

國立交通大學

電子物理研究所



A Thesis

Submitted to Department of Electrophysics
College of Science

National Chiao Tung University

In partial Fulfillment of the Requirements

For the Degree of

Master

in

Electrophysics

July 2004

Hsinchu, Taiwan, Republic of China

中華民國九十四年七月

To My Family and H. L.



具平面式與嵌入式電極的氮化鎵 金屬-半導體-金屬光偵測器之製作與光電特性量測

研究生: 蔡東昇

指導教授: 楊賜麟 博士

國立交通大學電子物理研究所碩士論文

中文摘要



我們在無參雜的氮化鎵(GaN)基板上製作出柵狀結構之紫外光金屬-半導體-金屬(MSM)光偵測器。我們設計了不同電極寬度及電極間距組合的 MSM 光偵測器，用以探討分析各種暗電流、光電流傳導機制及光響應頻譜。

在製程上，我們以白金為電極材料，分別製作出平面式電極與嵌入式電極的 MSM 光偵測器。在元件特性量測上，我們分別量測了元件的暗電流、光電流與光響應頻譜。我們發現在平面式電極的 MSM 之暗電流主要由表面漏電流所主導，而嵌入式電極的 MSM 之暗電流主要由內部漏電流所主導。製作出的氮化鎵 MSM 光偵測器的光響應範圍在 310 ~ 370 nm 之間。嵌入式電極的 MSM 光偵測器對波長為 360 nm 的光有最大響應度為 0.019 A/W，而平面式電極的 MSM 光偵測器在 360 nm 處有最大響應度為 0.009 A/W。

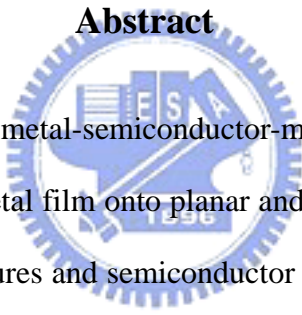
Fabrication and Optoelectronic Characterization of Planar and Recessed-Electrode GaN Metal-Semiconductor-Metal Photodetectors

Student: Dung-Sheng Tsai

Advisor: Dr. Su-Lin Yang

Department of Electrophysics
National Chiao Tung University

Abstract



We fabricated ultraviolet metal-semiconductor-metal (MSM) photodetectors by depositing interdigitated Pt metal film onto planar and recessed undoped-GaN wafers. Various metal electrode structures and semiconductor surface processing were used to investigate the conduction mechanism of dark currents and photocurrents of GaN MSM photodetectors.

We characterized the current-voltage relationships and spectrum responsivities of MSM photodetectors. We found that dark current is dominated by the surface leakage current for the planar MSM detectors and is dominated by the internal leakage current for the recessed-electrode MSM detectors. The photosensitive spectrum range is between 310 nm and 370 nm. For these GaN MSM detectors The peak responsivity of the planar MSM detectors is 0.009 A/W at 360 nm, while the peak responsivity of the recessed-electrode MSM detectors is 0.019 A/W at 360nm.

Contents

中文摘要	i
英文摘要	ii
致謝	iii
Contents	v
Chapter 1 Introduction	1
1.1 The development of photodetector	1
1.2 The GaN metal-semiconductor-metal photodetector	3
Chapter 2 Basic Theory of Metal-Semiconductor-Metal (MSM) Photodetector	5
2.1 Metal-semiconductor junction	5
2.1.1 Schottky contact	5
2.1.2 Ohmic contact	8
2.2 The current transport in the a metal-semiconductor junction	10
2.3 Metal-semiconductor-metal photodetector	14
2.3.1 Dark current of metal-semiconductor-metal photo detectors	15
2.3.2 Photo current of metal-semiconductor-metal	18
2.4 Responsivity	19
Chapter 3 Fabrication Process and Measurement Techniques for the MSM Photodetectors	21
3.1 Design and layout of photo mask	21
3.2 Fabrication processes	22
3.2.1 Wafer initial cleaning	22
3.2.2 Finger metal deposition	23
3.2.2.1 convential contact	23
3.2.2.2 recessed contact	24
3.2.3 Passivation and contact opening	25
3.2.4 Bonding pad metallization	26
3.3 I-V measurement	27

3.4 Measurement of spectrum response	27
Chapter 4 Results and Discussion	30
4.1 Process results of GaN MSM photodetectors	30
4.2 Dark current of GaN MSM photodetectors	32
4.3 Photo current of GaN MSM photodetectors	38
4.4 Photo response of GaN MSM photodetectors	42
Chapter 5 Conclusion	47
Reference	48



Chapter 1

Introduction

In this study, we investigated metal-semiconductor-metal (MSM) photodetectors (PDs). We fabricated MSM PDs with various metal geometric structures, planar and recessed contacts to study the optoelectronic characterization of MSM PDs, such as dark current, photo current, spectrum responsivity.

1.1 the development of photodetector

The birth of photodetectors can be dated back to 1873 when W. Smith discovered photoconductivity in selenium. Progress was slow until 1905, when Einstein explained the newly observed photoelectric effect in the metals, and Planck solved the blackbody emission puzzle by introducing the quanta hypothesis [2].

Application and new devices soon flourished, pushed by the dawning technology of television. In 30 years photoelectric vacuum-tubes covering all the fields of detection were developed, including the orthicon – the father of modern image pickup devices, the image converters and intensifiers, and the photomultiplier which technically survives today as the sole photodetector capable of single-photon detection, and is the key device for probing elusive nuclear particles such as solar neutrinos.

After World War II, semiconductor devices were invented, as a result of the improved understanding of their physics along with an adequate control of their technology. As technical fallout, a number of solid-state photodetectors were developed with improved performance, spectral coverage, reliability and size. These have made possible new application in instrumentation and communication.

We can distinguish two classes of photodetectors (Table1) [1] according to the handling of received power: *signal-element* photodetectors are those yielding an output signal proportional to the total (or integral) power collected by the active area. *Image* photodetector

are those with an active area physically or virtually divided in a string (1-D) or array(2-D) of individual elements (also called pixels from picture element), whose signals can be properly organized to be readable at the output port.

Photodetectors are further classified according to the type of optical to electrical conversion effect. The most important is the photoelectric effect, by which a photon(or quantum of energy $h\nu$) is absorbed by the material with the release of an electron-hole pair. If the photogenerated electron is further emitted out of the material, becoming available for collection or multiplication, the device is called a photoemission device or one based on the external photoelectric effect. Instead, if no emission takes place but the photogenerated electron-hole pair is available for the current circulation in the external circuit, we talk of an internal photoelectric effect or device. The table 1 is the synopsis of photodetectors and their spectral ranges.



1.2 the GaN metal-semiconductor-metal photodetector

Gallium nitride (GaN) is a wide band-gap ($\sim 3.4\text{eV}$) semiconductor that has received renewed interest based on recent advances in crystal growth and optoelectronic device fabrication such as light emitting diodes (LEDs) and laser diodes (LDs) in the blue and violet light region [3-6]. GaN is also highly promising for fabricating electronic devices operating at high temperatures of at least $300\text{ }^{\circ}\text{C}$ owing to their superior physical properties such as direct, wide band gap, high breakdown field, and high thermal conductivity. These properties make it an ideal choice for use in various detector applications such as ultraviolet (UV) astronomy, flame detection, biological and chemical detection, and engine monitoring where harsh working environments exploit the nature durability and visible blindness of the material. Although silicon is the semiconductors most commonly used for UV photodetectors due to its well-established technology. However, the use of wide band-gap semiconductors such as

diamond, silicon carbide (SiC), GaZ and Zinc selenium (ZnSe), make it possible to avoid filters and reduce aging effects.

In the past years, various types of GaN-based photodetectors have been proposed, such as p-n junction diodes, p-i-n diodes, p- π -n diodes, Schottky barrier diodes, and metal-semiconductor-metal (MSM) photodetectors (PDs). The MSM structure consists of a semiconductor absorbing layer on which two interdigitated electrode have been deposited to form back to back Schottky diodes (photovoltaic operation).[7-9]

The MSM structure is an attractive candidate for UV photodetectors because of its fabrication simplicity, the need for only a single-dopant active layer; and the potential to achieve high quantum efficiency, low internal gain, very low dark current. Moreover, extremely low noise densities have been reported in the MSM PDs and the fabrication process of MSM photodetector structure is compatible with field-effect-transistor (FET)-based electronics.[9-11] Thus, one can easily integrate GaN MSM PDs with GaN FET-based electronics to realize GaN-based optoelectronic integrated circuits (OEICs).

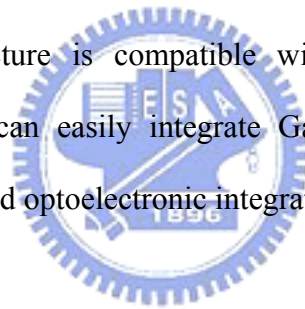


Table 1 the synopsis of photodetectors and their spectral ranges.

SPECTRAL RANGES				
$0.1 \mu\text{m}$	$1 \mu\text{m}$	$10 \mu\text{m}$	$100 \mu\text{m}$	(λ)
<i>-----photoemission-----</i>				
<i>-----internal photoelectric effect-----</i>				
<i>-----thermal-----</i>				

	<i>Single element</i>	<i>Image</i>
<i>-photoemission devices</i> <i>(or external photoelectric devices)</i>	vacuum photodiode gas photodiodes photomultiplier	pickup tubes image intensifiers and converters
<i>-internal photoelectric devices</i>	semiconductor photodiodes avalanche photodiode phototransistor (BJT,FET) photoresistance	CCDs
<i>-thermal detectors</i>	thermocouple(or photopile) thermistor(or bolometer) pyroelectric	vidicon
<i>-weak interaction detectors</i>	photon drag, Golay cell photoelectromagnetic point contact diode	uncool IR FPA IR vidicon



Chapter 2

Basic theory of MSM detector

2.1 Metal-semiconductor junction

2.1.1 Schottky contact

The ideal energy diagram for a particular metal and n-type semiconductor before marking contact is shown in Fig.2.1. The vacuum level is a reference level. The parameter ϕ_m is the metal work function (measured in volts), ϕ_s is the semiconductor work function, and χ is known as the electron affinity. We have assumed that $\phi_m > \phi_s$. Before contact, the Fermi level in the semiconductor was above that in the metal. In order for the Fermi level to become a constant through the system in the thermal equilibrium, electrons from the semiconductor flow into the lower energy states in the metal. Positively charged donor atoms remain in the semiconductor, creating a space charge region. After contact, the ideal energy-band diagram of a metal-n-semiconductor junction for $\phi_m > \phi_s$ is shown in Fig.2.2. The parameter ϕ_{B0} is the ideal barrier height of the semiconductor contact, the potential barrier seen by electrons in the metal trying to move into the semiconductor. [12]

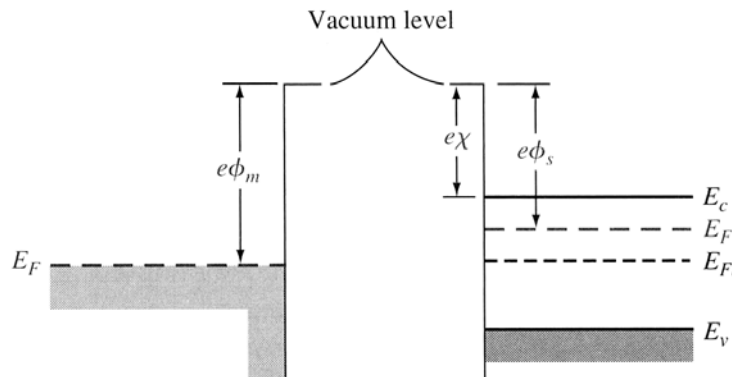


Fig. 2.1 Energy-band diagram of a metal and semiconductor before contact

The barrier is known as the Schottky barrier and is given, ideally, by

$$\phi_{B0} = (\phi_m - \chi)$$

On the semiconductor side, V_{bi} is the built-in potential barrier. The barrier, similar to the case of the pn junction, is the barrier seen by electrons in the conduction band trying to move into the metal. The built-in potential barrier is given by

$$V_{bi} = \phi_{B0} - \phi_n$$

which make V_{bi} a slight function of the semiconductor doping, as was the case in a pn junction.[12-13]

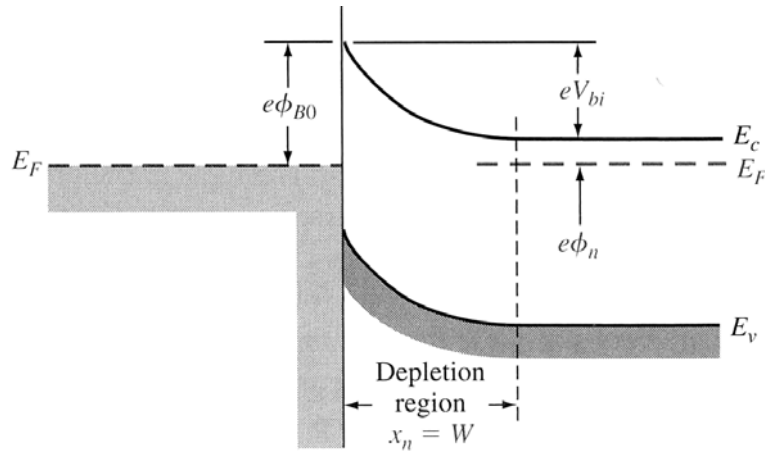


Fig 2.2 Ideal energy-band diagram of a metal-n-semiconductor junction

for $\phi_m > \phi_s$.

If we apply a positive voltage to the semiconductor with respect to the metal, the semiconductor-to-metal barrier height increases, while ϕ_{B0} remains constant in this idealized case. This bias condition is the reverse bias. If a positive voltage is applied to the metal with respect to the semiconductor, the semiconductor-to-metal barrier V_{bi} is reduce while ϕ_{B0} again remains essentially constant. This bias condition is the forward bias. The energy-band diagrams for the reverse and forward bias are shown in Fig.2.3 and 2.4.

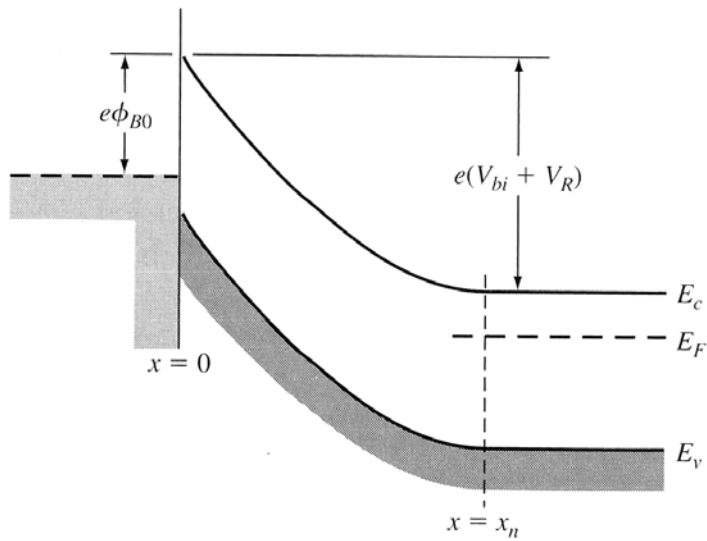


Fig.2.3 Ideal energy-band diagram of a metal-semiconductor junction under the reverse bias.

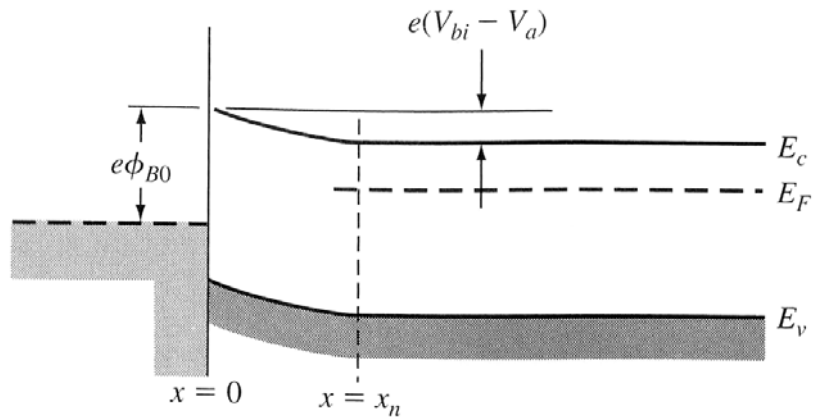


Fig.2.4 Ideal energy-band diagram of a metal-semiconductor junction under the forward bias.

2.1.2 Ohmic contact

Ohmic contacts are metal-to-semiconductor contacts, but in this case they are not rectifying

contacts. An ohmic contact is a low resistance junction providing conduction in both directions between the metal and the semiconductor. Two general types of ohmic contacts are possible: the first type is the ideal nonrectifying barrier, and the second is the tunneling barrier. We will define a specific contact resistance that is used to characterize ohmic contacts. In Fig.2.5 for a case when $\phi_m < \phi_s$ we see the energy levels before contact and, in Fig. 2.6, the barrier after contact for thermal equilibrium in this junction. To achieve thermal equilibrium in this junction, electrons will flow from the metal into the lower energy states in the semiconductor, which makes the surface of the semiconductor more n type. The excess electron charge in the n-type semiconductor exists essentially as a surface charge density. If a positive voltage is applied to the metal, there is no barrier to electrons flowing from the semiconductor into the metal. If a positive voltage is applied to the semiconductor, the effective barrier height for electrons flowing from the metal into the semiconductor will be approximately $\phi_{Bn} = \phi_n$, which is fairly small for moderately to heavily doped semiconductor. For this is bias condition, electrons can easily flow from the metal into the semiconductor.[12-13]

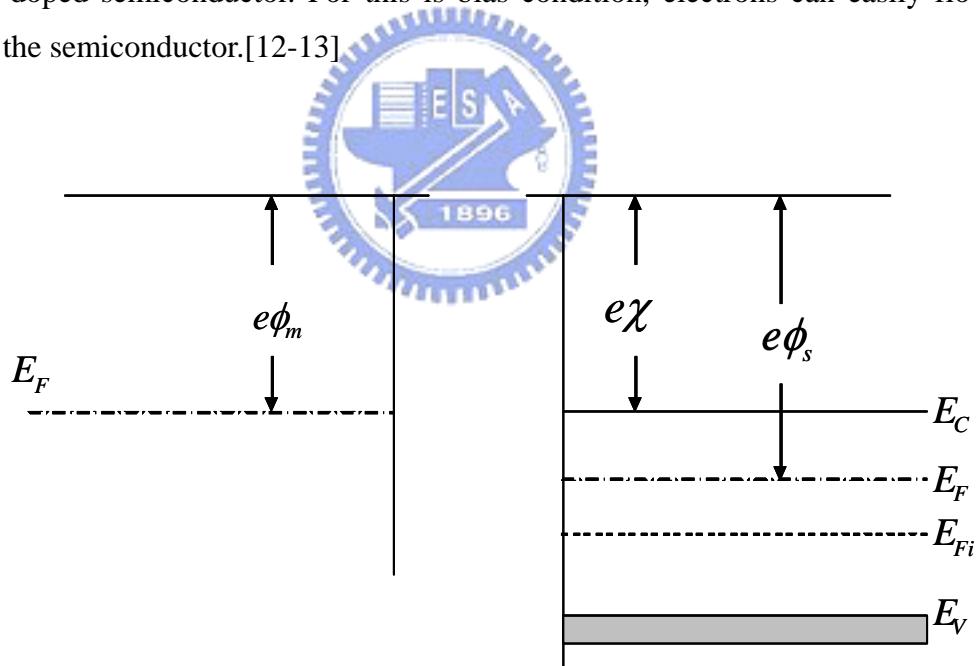


Fig.2.5 Ideal energy-band diagram before contact for a metal-n-semiconductor junction for $\phi_m < \phi_s$.

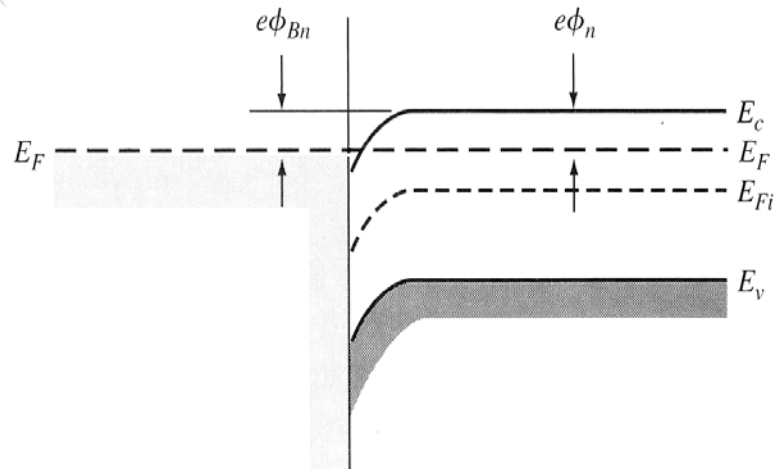


Fig.2.6 Ideal energy-band diagram after contact for a metal-n-semiconductor junction for $\phi_m < \phi_s$.

Fig. 2.7(a) shows the energy-band diagram when a positive voltage is applied to the metal with respect to the semiconductor. Electrons can easily flow “downhill” from the semiconductor into the metal. Fig. 2.7(b) shows the case when a positive voltage is applied to the semiconductor with respect to the metal. Electrons can easily flow over the barrier from the metal into the semiconductor. This junction, the, is an ohmic contact.

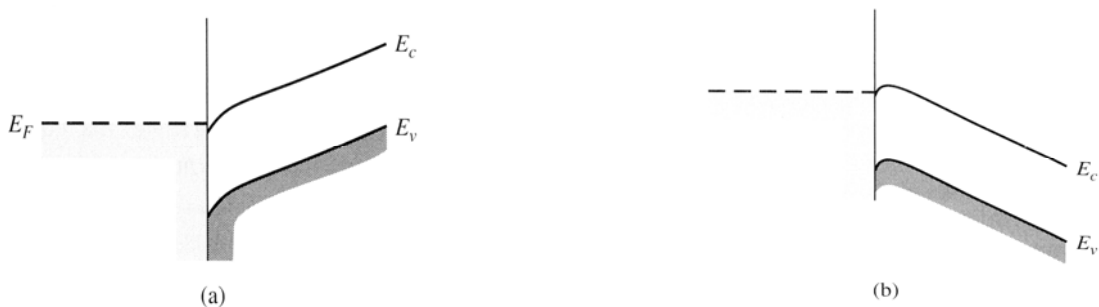


Fig. 2.7 Ideal energy-band diagram of a metal-n-semiconductor ohmic contact (a) with a positive voltage applied to the metal and (b) with a positive voltage applied to the semiconductor.

2.2 The current transport in the a metal-semiconductor junction

After particular metal and semiconductor making contact, the interface will form a barrier. This contact is a rectifying contact and is called for Schottky contact. On the other hand, Ohmic contacts are not rectifying contacts and low-resistance junction providing conduction in both directions between the metal and semiconductor. The current transport in a metal-semiconductor junction is due mainly to majority carriers as opposed to minority carriers in a pn junction. The four mechanisms of current transport in the metal-semiconductor junction are as follows. (1) thermionic emission (TE), (2) thermionic field emission(TFE), (3) generation-recombination, (4) minor carrier injection.

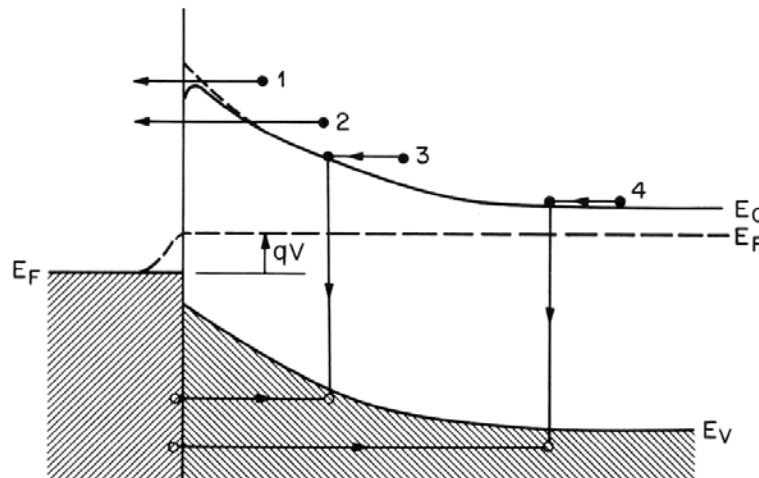


Fig 2.9 The four mechanisms of current transport in the metal-semiconductor junction (1) thermionic emission(TE), (2) thermionic field emission(TFE), (3) generation-recombination, (4) minor carrier injection.

After the schottky metal and n-type semiconductor with different carrier concentrations making contact, the interface can form different barrier heights. The electron will go through these barrier heights by different ways and produce several current transport mechanism. These mechanisms include thermionic emission, thermionic field emission, and field emission.[12-15]

(1) thermionic emission

The thermionic emission characteristics are derived by using the assumptions that the barrier height is much larger than kT , so that the Maxwell-Boltzmann approximation applies and that thermal equilibrium is not affected by this process. Fig. 2.10 shows the one-dimensional barrier with an applied forward-bias voltage V_a and shows two electron current density components. The current $J_{s \rightarrow m}$ is the electron current due to the flow of electron from the semiconductor into the metal, and the current $J_{m \rightarrow s}$ is the electron current density due to the flow of electrons from the metal into semiconductor. The subscripts of the currents indicate the direction of electron flow. The conventional current direction is opposite to the electron flow. The net current density in the metal-to-semiconductor junction can be written as

$$J = J_{s \rightarrow m} - J_{m \rightarrow s} \dots\dots\dots (2.1)$$

which is defined to be positive in the direction from the metal to the semiconductor.

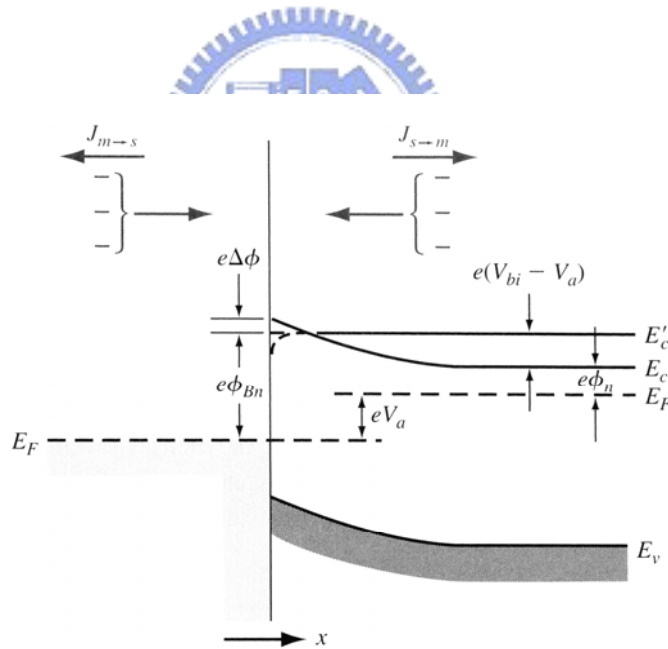


Fig.2.10 Energy-band diagram of a forward-biased metal-semiconductor junction including the image lowering effect.

We find that

$$J = \left[A^* T^2 \exp\left(\frac{-e\phi_{Bn}}{kT}\right) \right] \left[\exp\left(\frac{eV_a}{kT}\right) - 1 \right] \dots\dots\dots (2.2)$$

where

$$A^* \equiv \frac{4\pi m_n^* k^2}{h^3}$$

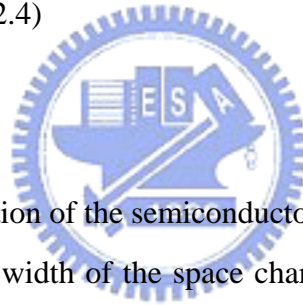
The parameter A^* is called the effective Richardson constant for thermionic emission.

Equation (2.2) can be written in the usual diode form as

$$J = J_{sT} \left[\exp\left(\frac{eV_a}{kT}\right) - 1 \right] \dots\dots\dots (2.3)$$

Where J_{sT} is the reverse-saturation current density and is given by

$$J_{sT} = A^* T^2 \exp\left(\frac{-e\phi_{Bn}}{kT}\right) \dots\dots\dots (2.4)$$



(2) thermionic field emission

When the doping concentration of the semiconductor achieves the range, $10^{17} \text{ cm}^{-3} < N_d < 10^{18} \text{ cm}^{-3}$, the width of the space charge region in the semiconductor is still enough to avoid the electron tunneling directly. If some of the electrons have a few energy, these electrons still tunnel the space charge region. We know that the mechanisms of thermionic emission and tunneling always occur at the same time. When the probability of the tunneling is large to dominate the Schottky contact transport, we call this situation as thermionic field emission. We can write down the I-V relation.

$$J = J_s \exp(E/E_0) \dots\dots\dots (2.5)$$

Where

$$J_s = \frac{A\pi^{1/2} E_{00}^{1/2} (E_B - E + \xi_2)^{1/2}}{kT \cosh(E_{00}/kT)} \times \exp\left[\frac{\xi_2}{kT} - \frac{E_B + \xi_2}{E_0}\right],$$

$$E_{00} = \frac{qh}{2} \sqrt{\frac{N_d}{\epsilon_s m_n^*}}, \quad E_0 = E_{00} \coth\left(\frac{E_{00}}{kT}\right)$$

ξ_2 is the energy of the Fermi level of the semiconductor measured with respect to the bottom of

its conduction band. E is the potential energy associated with an applied bias V between the metal and the semiconductor. E_B is the potential energy of the top of the barrier with respect to the Fermi level of the metal. A is the classical Richardson constant for the semiconductor.[15]

$$A = \frac{4\pi m^* q (kT)^2}{h^3}$$

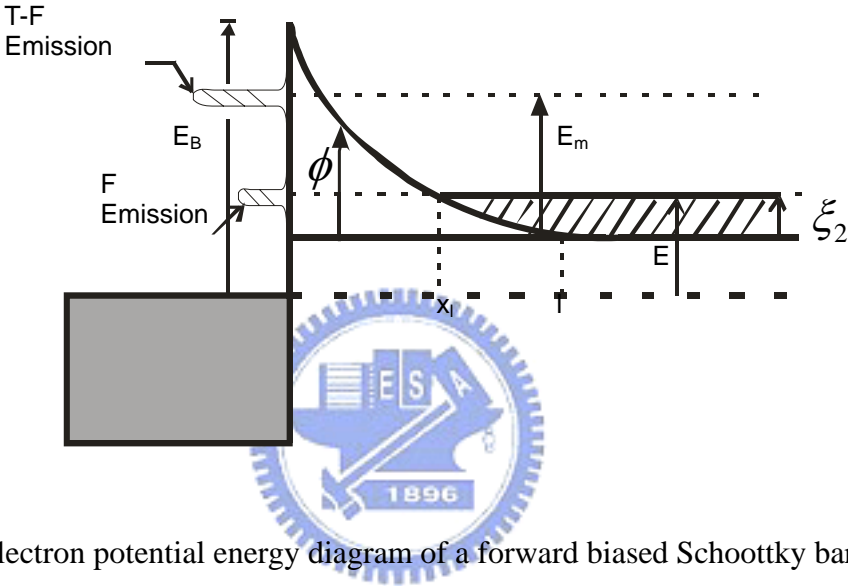


Fig. 2.11 electron potential energy diagram of a forward biased Schottky barrier.

(3) field emission

In the heavily doping semiconductor ($N_d \geq 10^{18} \text{ cm}^{-3}$), the width of space charge region becomes more narrow. The electron will more easily tunnel form the metal to the semiconductor or from the semiconductor to the metal. This phenomenon is called as field emission. According to the literature, we fine the approximation equation for the I-V relation. [15]

$$J_t = \exp\left[\frac{-q\Phi_{bi}}{E_{00}}\right] \dots \dots \dots (2.6)$$

J_t : field emission current density.

2.3 Metal-semiconductor-metal photodetector

A Metal-semiconductor-metal (MSM) photodetector is simply composed of two back-to-back Schottky diodes and has interdigitated electrodes on an active light absorption (active) layer as shown in Fig.2.12.

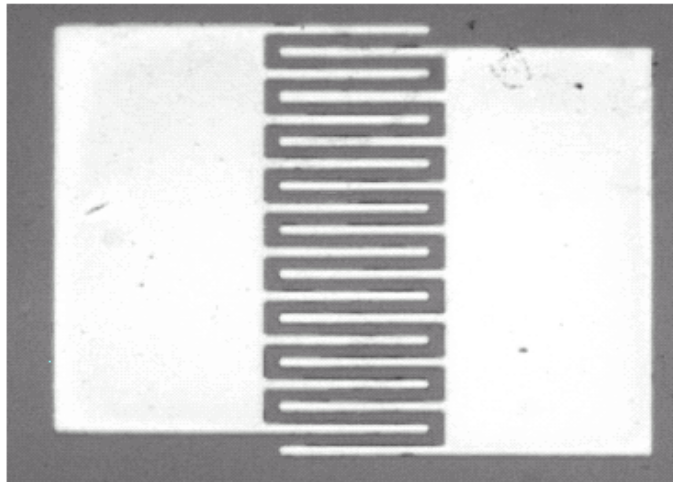


Fig. 2.12 A schematic of MSM detector using interdigitated Schottky contact.

An MSM photodetector is inherently planar and requires only a single photolithography step that is compatible with existing field effect transistor (FET) technology. MSM photodetectors are very high-speed devices due to their low capacitance, and they typically have very low dark currents (current produced without incident light). However, the responsivity (total signal produced from a given optical input) is quite low compared to p-i-n photodiodes.[4-6] The main causes for the low responsivity is the reflection from the surface metals and semiconductor surface, the finite carrier lifetime as the carriers traverse the gap between the electrodes before being collected, absorption of incident light outside the region in which photo generated carriers can be collected by the electrodes, and surface recombination currents and deep traps within the semiconductor material which may lower the detected optical signal.

2.3.1 Dark current of metal-semiconductor-metal photo detectors

Forming two Schottky contacts on an undoped semiconductor layer makes the MSM photo detector. It can be designed such that the region in between is almost completely depleted. In a planar configuration the two Schottky contacts are made of Ni/Au, Pt/Au, Ti/Pt, or Pt. These can be single contacts, or interdigitated, as show in Fig. 2.12. with a contact spacing of 2, 3, 4, 5, or 8. The band diagram of the MSM photo detector with an applied bias V_a is shown in Fig.2.13. The ϕ_{nb1} and ϕ_{nb2} are the electron barrier heights for contacts 1 and 2 respectively. Under an applied voltage, one of the contacts called the contact No.1 is reverse bias and the other, called contact No.2, is forward bias. As the applied voltage increase, the sum of the two depletion widths also increases. Eventually at the reach-through voltage, V_{RT} , the two depletion regions touch each other.[14]

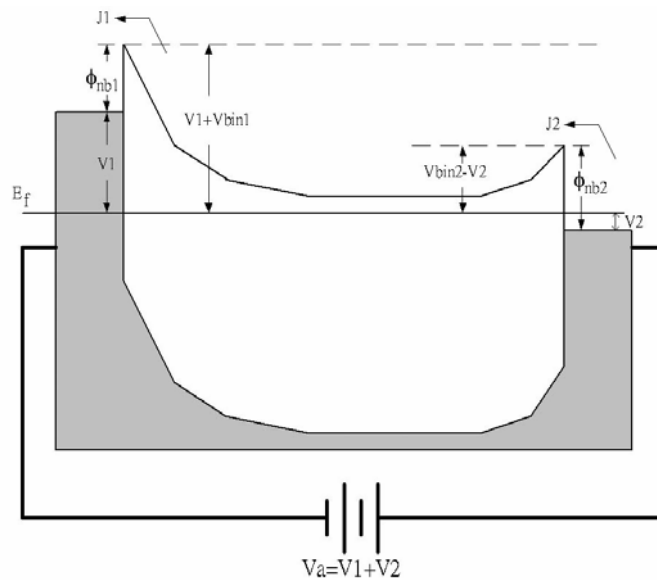


Fig.2.13 The band diagram of the MSM photo detector with an applied bias V_a .

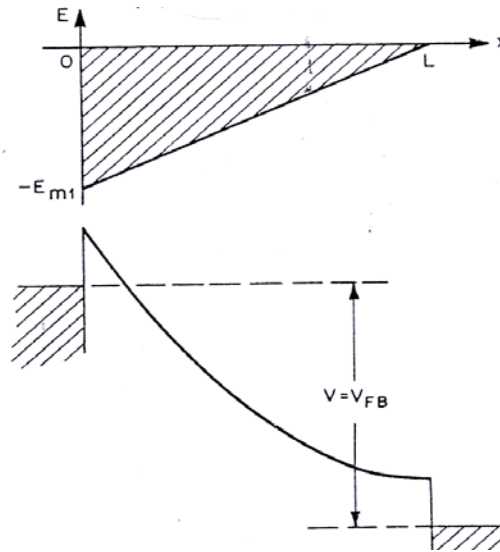


Fig.2.14 Condition of flat-band at which the energy band at X=L becomes flat. The corresponding voltage V_{FB} is called flat-band voltage.

As the voltage increase further, a point is reached at which the electric field at $x=L$ becomes zero and the energy band at $x=L$ become flat. This is the flat-band condition with the corresponding flat-band voltage, V_{FB} , shown in Fig.2.14. The flat-band voltage V_{FB} can be expressed as

$$V_{FB} = \frac{qN_d W^2}{2\epsilon_s \epsilon_0} \dots\dots\dots (2.7)$$

where two dimensional effects are ignored. Here W is the electrode spacing and N_D is the donor density in the n-type layer.[13-14]

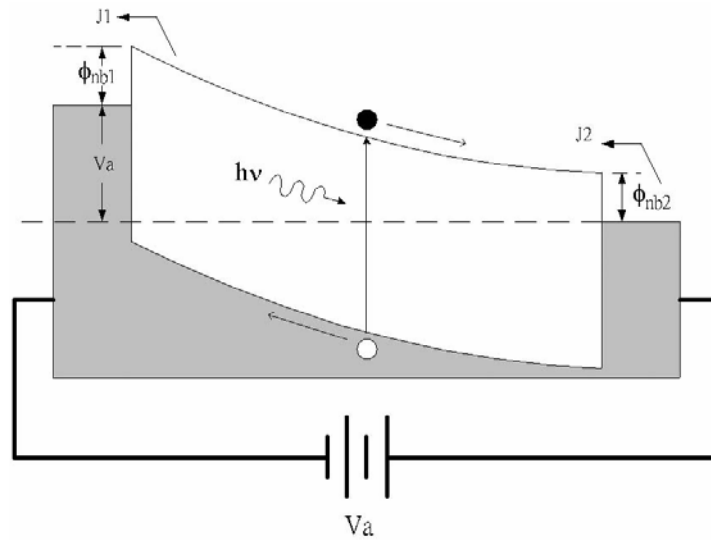


Fig.2.15 The band diagram of the MSM photo detector with $V_a > V_{FB}$.

The dark current of the device is principally determined by thermionic emission over the barrier. With respect to Fig.2.13, at low biases electron injection at the reverse bias contact is the dominant conduction mechanism. As the bias increases hole injection tends to dominate after the reach-through condition (the two depletion edges coincide) is reached. The total current density under these conditions is therefore given by

$$J = A_n^{**} T^2 \exp\left\{-q \frac{(\phi_{bn} - \Delta\phi_{bn})}{k_B T}\right\} + A_p^{**} T^2 \exp\left\{-q \frac{(\phi_{bp} - \Delta\phi_{bp})}{k_B T}\right\} \dots \dots \dots (2.8)$$

where the A_n^{**} is the respective Richardson constants and the $\Delta\phi$ is the respective barrier height lowering due to the image force effect, shown in Fig. 2.16.[14]

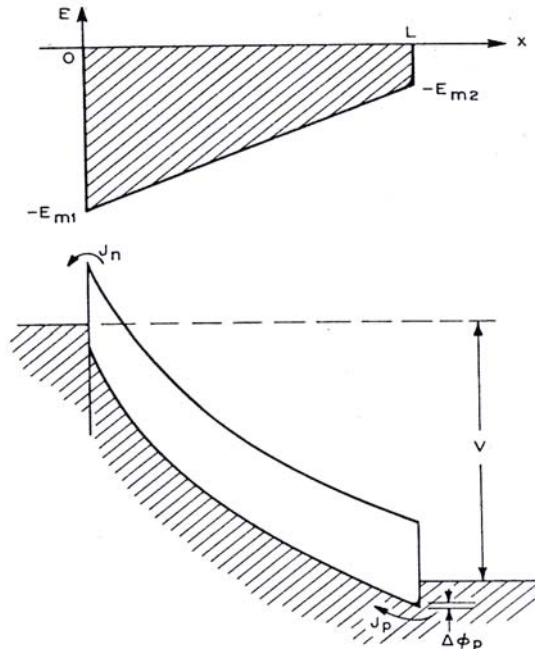


Fig. 2.16 Condition for applied voltage larger than V_{FB} , $\Delta\phi_p$ is the image-force lowering of ϕ_{p2} .



2.3.2 Photo current of metal-semiconductor-metal

To illuminate the MSM photo detector in the light source ($E > E_g$), it will exhibit photocurrent. Considering one dimension model, g is generating rate of semiconductor then photocurrent density J is

$$J = -qg(W_1 + L_p) + qg(W_2 + L_{anode}) \quad \text{for } x_2 - x_1 \gg L_p \dots\dots\dots (2.9)$$

Where L_p is diffusing length of the hole in depletion near cathode, and L_{anode} is diffusing length of the hole in depletion near anode.

2.4 Responsivity

The definition of photodetector's responsivity is the ratio of incident light power to induced photocurrent. Take account of the cause of gain, MSM photodetector responsivity can be represented as

$$R = \frac{\eta_{ext}q}{hv} \Gamma_G \dots\dots\dots (2.10)$$

Where R is the responsivity, η_{ext} is external quantum effect, q is electron charge, h is plank's constant, v is the frequency of incident light and Γ_G is internal gain. In general, external quantum effect can be showed as

$$\eta_{ext} = \frac{S}{S+W} (1-R)(1-e^{-\alpha d}) \dots\dots\dots (2.11)$$

Where S means space width, W is finger width, R is surface reflectivity, α is absorption constant and d is the thickness of active layer. Another parameter Γ_G can be represented as follows

$$\Gamma_G = \frac{\mu_e + \mu_h}{\mu_e} \frac{\tau}{t_{tr}^e} \dots\dots\dots (2.12)$$

$$t_{tr}^e = \frac{S^2}{\mu_e V} \dots\dots\dots (2.13)$$

Where μ_e and μ_h is mobility of electron and hole, τ is the recombination time, t_{tr}^e is electron transmission time, S is space width and V is applied voltage.

The mobility difference of electron and hole induce this gain. Hole mobility is smaller than electron. When device is illuminated, electrons and holes produce in the conduction and valance band. Because of holes in valance band move much slower, when electrons in conduction band pass through semiconductor into metal, few holes in valance band still survived. In order to keep

the neutral of depletion region, the electrons in the cathode will inject into semiconductor and this is called gain. This result must be corrected by experiment. There is also the other phenomenon that the holes are trapped by acceptor states at the metal-semiconductor interface to lower the barrier height. The electrons would inject into the semiconductor from the cathode after lowering the barrier height so that the gain will be induced. [16-19]



Chapter 3

Fabrication Process and Measurement Techniques for the MSM photodetectors

In this chapter, fabrication processes and characterization techniques for the metal-semiconductor-metal (MSM) photodetectors are presented.

3.1 Design and layout of photo mask

We designed the MSM photodetector structures and the layout of mask patterns by using Tanner L-Edit. Three masks were used to fabricate various geometric structured GaN MSM photodetectors.

- (1) metal finger mask: Finger mask delineates the MSM fingers. The pattern of some sampled fingers is shown in Fig. 3.1.



Fig.3.1 The metal finger mask.

- (2) contact-opening mask: Contact-opening mask is used to open contact windows through the passivation layer to connect the finger metal with pad metal. The pattern of sampled contact openings corresponding to the fingers in Fig. 3.1 is shown in Fig. 3.2.



Fig.3.2 Contact-opening mask.

(3) padding mask: Padding mask delineates bonding pads. The pattern of sampled pads corresponding to the fingers in Fig. 3.1 is shown in Fig. 3.3.

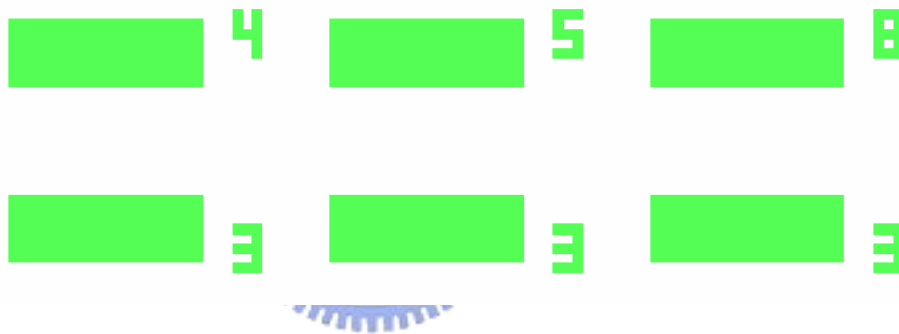


Fig.3.3 Padding mask.

3.2 Fabrication processes

We fabricated MSM photodetectors on un-doped GaN. The processes were performed at laboratory of Vtera Technology Inc., Science-Base Industrial Park, Hsinchu, Taiwan. To give clear illustration of fabrication procedures, some 3-D figures of processed sample are depicted accompanying with the following process descriptions.

3.2.1 Wafer initial cleaning

(1) Immersing in ACE for 10 min.

(2) Immersing in IPA for 5 min.

(3) Dipping in D.I water.

(4) Blowing with N₂.

3.2.2 Finger metal deposition

3.2.2.1 Conventional contact

(1) Baking at 120°C.

(2) Coating photoresist AZ5214 with spin rate of 500 rpm for 5 s and then 3500 rpm for 25 s.

(3) Soft baking at 100°C.

(4) UV exposing with the metal finger mask for 4 s.

(5) Post exposure baking at 120°C.

(6) Exposing with a UV light.

(7) Developing with FHD-5.

(8) Rinsing with D.I water.

(9) Blowing with N₂.

(10) After exposure inspection with optical microscope to observe lithographic results.

(11) Baking at 120°C

(12) Plasma etching the residual photoresist with O₂ for 30 s.

(13) E-gun evaporation of MSM interdigitated Schottky metals. Various kind of metal were chosen for this application

(14) Lifting off the unwanted metal.

(16) Observing the finger metals by using the microscope. (The temporally finished



sample structure is shown in Fig 3.4.)

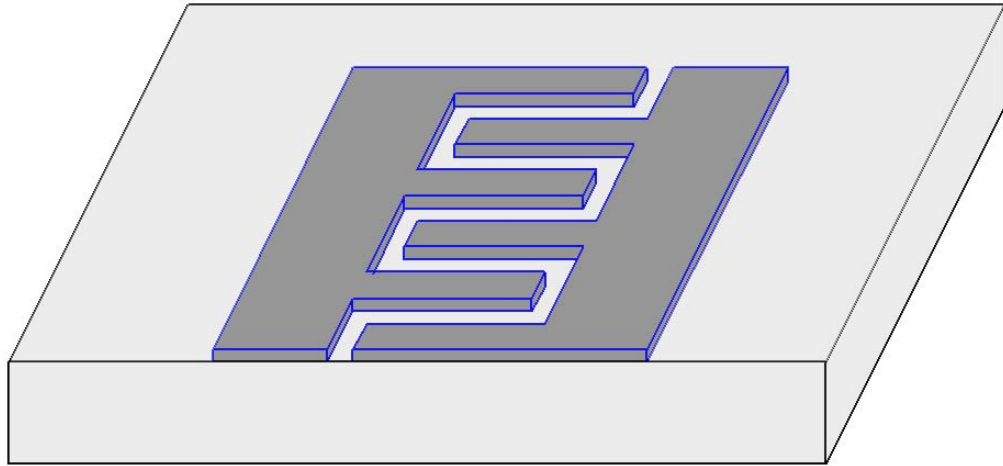


Fig.3.4 Stereo graph of the sample after finger metal preparation.

3.2.2.1 Recessed contact [19]

- (1) Baking at 120°C .
- (2) Coating photoresist AZ5214 with spin rate of 500 rpm for 5 s and then 3500 rpm for 25 s.
- (3) Soft baking at 100°C .
- (4) UV exposing with the metal finger mask for 4 s.
- (5) Post exposure baking at 120°C for 2 min.
- (6) Exposing with a UV light.
- (7) Developing with FHD-5.
- (8) Rinsing with D.I water.
- (9) Blowing with N₂.
- (10) After exposure inspection with optical microscope to observe lithographic results.
- (11) Baking at 120°C .



- (12) Plasma etching the residual photoresist with O_2 for 30 s.
- (13) Wet etching was performed to recess the sample to the depth of 100 angstrom.
- (13) E-gun evaporation of MSM interdigitated Schottky metals. Various kind of metal were chosen for this application
- (14) Lifting off the unwanted metal.
- (16) Observing the finger metals by using the microscope. (The section of the temporally finished sample structure is shown in Fig 3.5.)

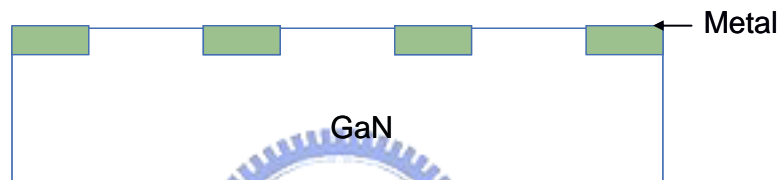


Fig 3.5 The schematic structure of the sample after recessed-electrode preparation.

3.2.3 Passivation and contact opening

- (1) Wafer cleaning with $H_2O:NH_4F:CH_3COOH = 120:1:1$ for 2 mins.
- (2) Deposit oxidation (SiO_2 , or Si_3N_4) with thickness of 2500 Å by plasma enhanced chemical vapor deposition (PECVD).
- (3) Photolithographic processes with contact-opening mask. The detailed procedures are the same to processes from (1) to (10) for finger metal deposition.
- (4) Etching oxidation (SiO_2 , or Si_3N_4) for opening by inductor coupled plasma (ICP) etching technique.
- (5) Photoresist removal with ultrasonic ACE and IPA.
- (6) Residual chemical removal and drying sample.

- (7) Observing the contact opening patterns by using the microscope. (The temporally finished sample structure is shown in Fig 3.6.)

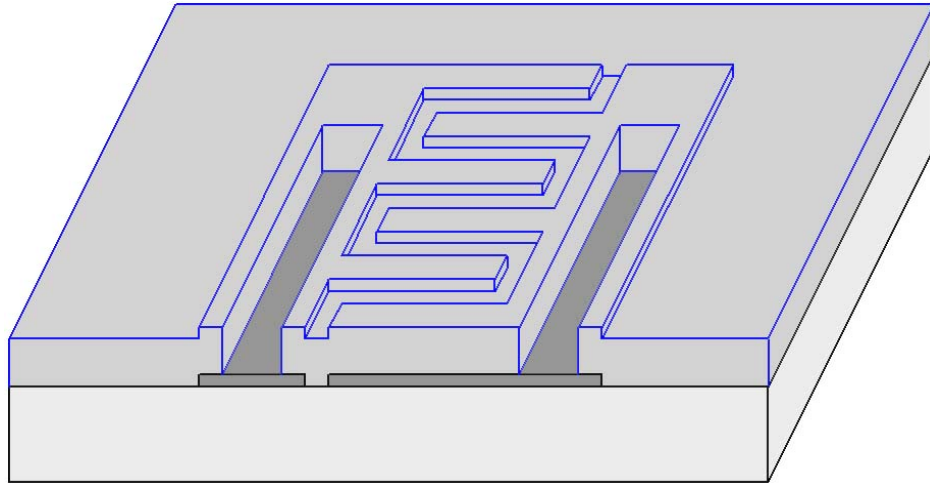


Fig.3.6 Stereo graph of the sample after contact opening.

3.2.4 Bonding pad metallization

- (1) Wafer cleaning.
- (2) Photolithographic processes with contact-opening mask. The detailed procedures are the same to processes from (1) to (10) for finger metal deposition.
- (3) Slightly plasma etching the residual photoresist with O_2 for 45 s.
- (4) Metallization of Ti-Al with E-gun evaporation technique.
- (5) Lift off the unwanted metal to form bonding pads connecting to finger metal.
- (6) Cleaning and drying sample.
- (7) Observing the pad patterns by using the microscope. (The finished sample structure is shown in Fig 3.7.)

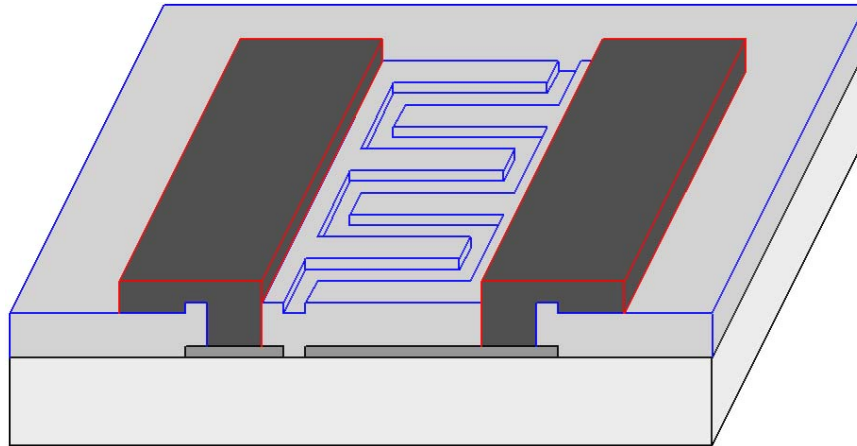


Fig.3.7 Stereo graph of the sample after the final process.

3.3 I-V measurement

Fig.3.8 illustrates the setup used for I-V measurement to characterize the performance of MSM photodetector, in term of dark currents and photo currents versus device bias voltage. Keithley source-measurement-unit 236 is used to measure the I-V characteristics of MSM detectors with/without He-Cd laser beam illumination. The measurement results were recorded for further analysis.

3.4 Measurement of spectrum response

The optoelectronic properties of MSM photodetector, such as photo current versus bias voltage under the monochromatic light illumination, were characterized. Fig. 3.9 shows the set up for the spectrum response measurement of MSM photodetectors.

Experimental setup:

1. Hg-Xe lamp: A light source of continuing wavelength.
2. HeCd laser: The wavelength is 325 nm and the power is 12.6 mW.
3. Monochromator: ARC SPECTRO-275 Monochromator with 27.5 cm focal length was used to extract nearly single wavelength light from the broad band Hg-Xe light

source to impinge on the MSM photodetectors.

4. lock-in amplifier: STANFORD RESEARCH SYSTEM SR850.

5. Digital voltage meter: HP 3478A which be used to measurement DC information.

8. pre-amplifier: STANFORD RESEARCH SYSTEM SR850. It is used to amplify the small signal current to a large voltage.

Fig 3.9 shows the spectrum response measurement setups of MSM. The light emitted from a Hg-Xe lamp is modulated by chopper to a special frequency. Through the monochromator, the light is separated to near single wavelength light which illuminates on the samples. The low current signal produced by devices is amplified to voltage signal and then was measured by a lock-in amplifier synchronized with the modulated frequency.

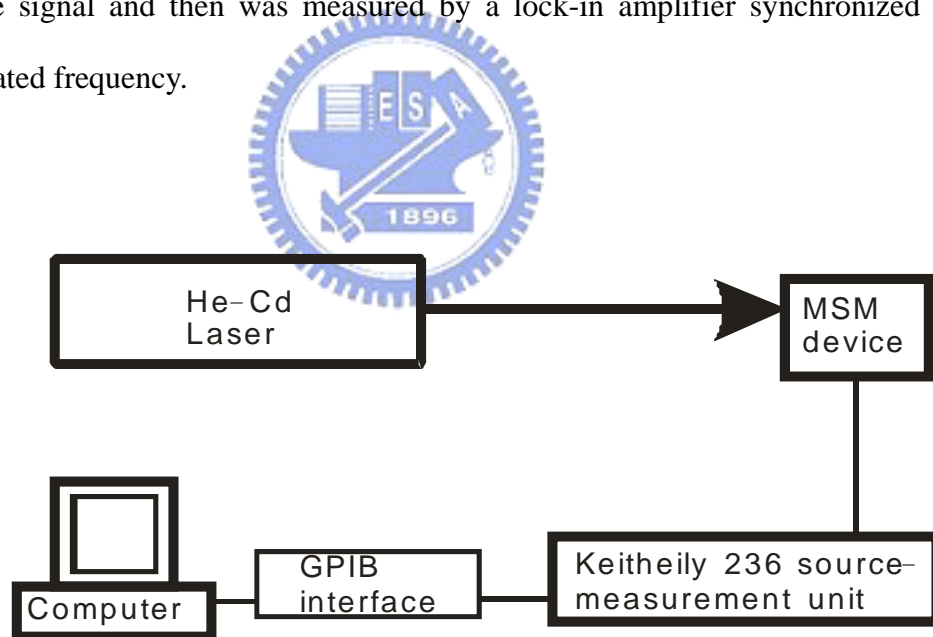


Fig 3.8 Setup of dark and photo current measurement for MSM photodiodes.

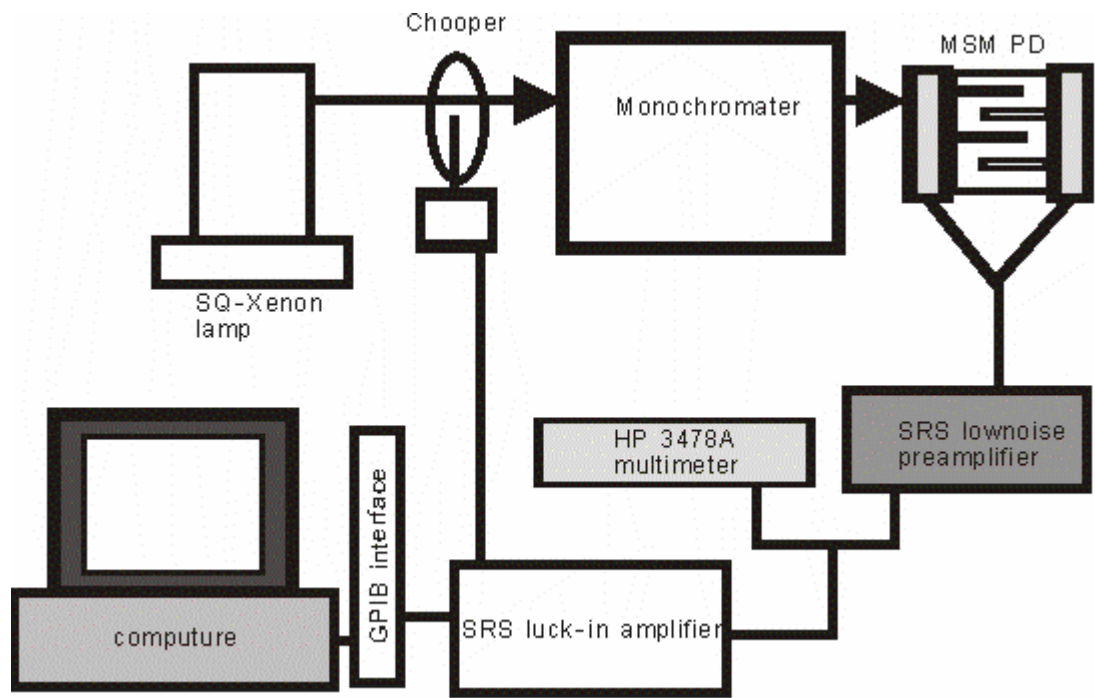


Fig 3.9 Setup of spectral responsivity for MSM photodiodes.



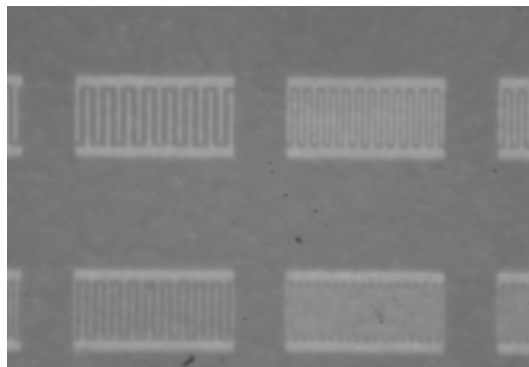
Chapter 4

Results and Discussion

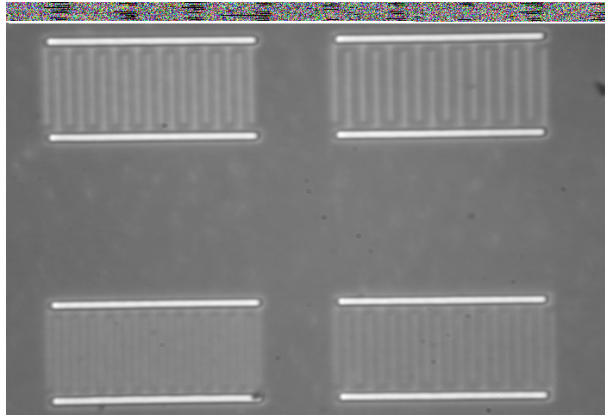
In this chapter, the fabrication process results and optoelectronic characteristics of metal-semiconductor-metal photodetectors (MSM-PDs) are presented. Dark current and photocurrent of MSM-PDs of various geometric structures are measured and analyzed. The factors determine the dark and photo currents of MSM-PDs are discussed. Spectrum responsivity of MSM-PDs was measured to confirm the UV detection capabilities of these GaN MSM-PDs.

4.1 Process results of GaN MSM photo detector

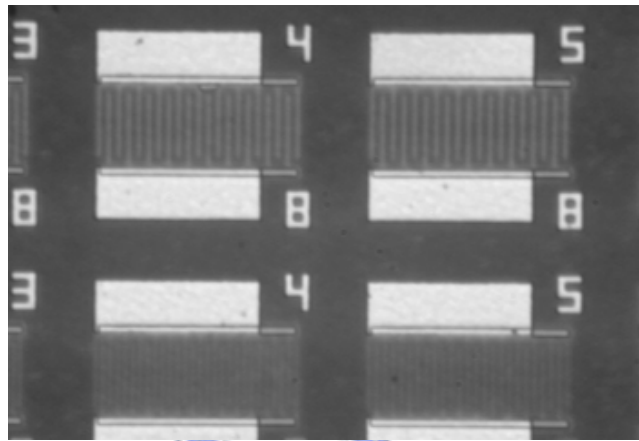
We have successfully fabricated MSM-PDs on GaN. Fig. 4.1 (a)-(c) show the photographs of samples after processes (a) finger metal deposition, (b) contact opening, and (c) bonding pad metallization, respectively, by optical microscopy.



(a)



(b)



(c)

Fig 4.1 Photographs of samples after processes (a) finger metal deposition, (b) contact opening, and (c) bonding pad metallization.

In our design, there are 20 different geometry sets of MSM-PDs. For the interdigit metal finger structure, we made various MSM-PD chips with a finger width of 3, 4, 5, or 8 μm and with a finger spacing of 2, 3, 4, 5, or 8 μm , and all with the same chip area of $250 \times 250\mu\text{m}^2$. We also fabricated the MSM-PDs with the recessed electrodes. For distinguishing the device geometric structures, sample #sw is adopted to denote the MSM-PD detector with $s\mu\text{m}$ spacing and $w\mu\text{m}$ finger width. i.e., sample 38 has 3 μm finger spacing and 8 μm finger width.

4.2 Dark current of GaN MSM photodetectors

Theoretically, the dark current of the MSM photodetectors consists of surface leakage current and the internal leakage current (reverse saturation current). Fig.4.2 shows the two main mechanisms for leakage currents of the MSM PDs. We use the simple concept to analyze our experimental results and to induce the relation between dark current and different geometric structured MSM-PDs.

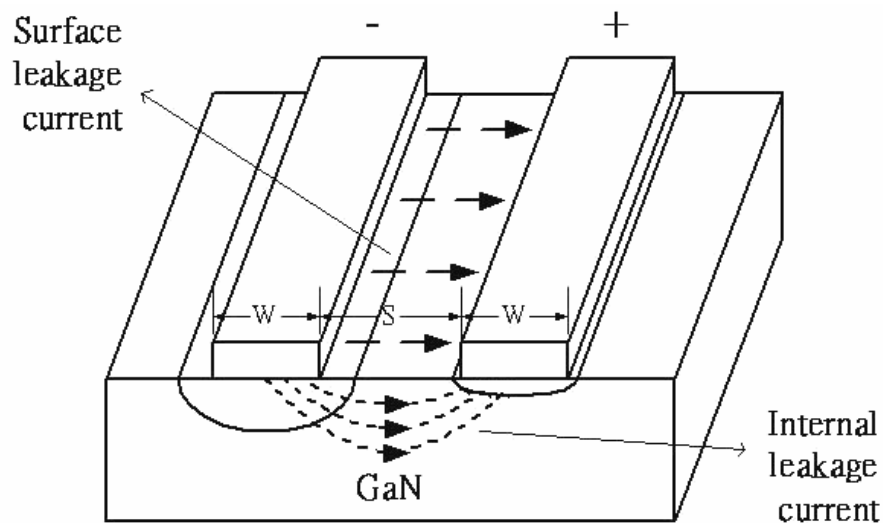


Fig 4.2 illustrates two ways for leakage currents

According to the formerly research results of our group, we have found that Pt is a suitable metal to be made the electrode in the GaN MSM-PDs.[20] In this study, Pt is selected for the metal material in the MSM structure. Fig.4.3 shows the dark I-V characteristics of the conventional and recessed-electrode GaN MSM-PDs with or without oxidation. With oxidation, it was found that the dark currents were $57\mu\text{A}$ and $0.4\mu\text{A}$ for the MSM-PDs with and without recessed electrodes under 20V bias. Without oxidation, it was found that dark currents were $96\mu\text{A}$ and $28\mu\text{A}$ for the MSM-PDs with and without recessed electrodes under 20V bias. The large leakage current observed in MSM-PD with recessed electrodes is

attributed to the wet etching induced surface damages. From these I-V curves, it should be noted that the dark current of MSM-PDs with recessed electrodes reaches saturation faster than that of MSM-PDs without recessed electrodes. At the same time, we also found the smaller dark current of MSM PDs with oxidation. The dark current of MSM PDs with passivation layer is lower because of the lower surface density.

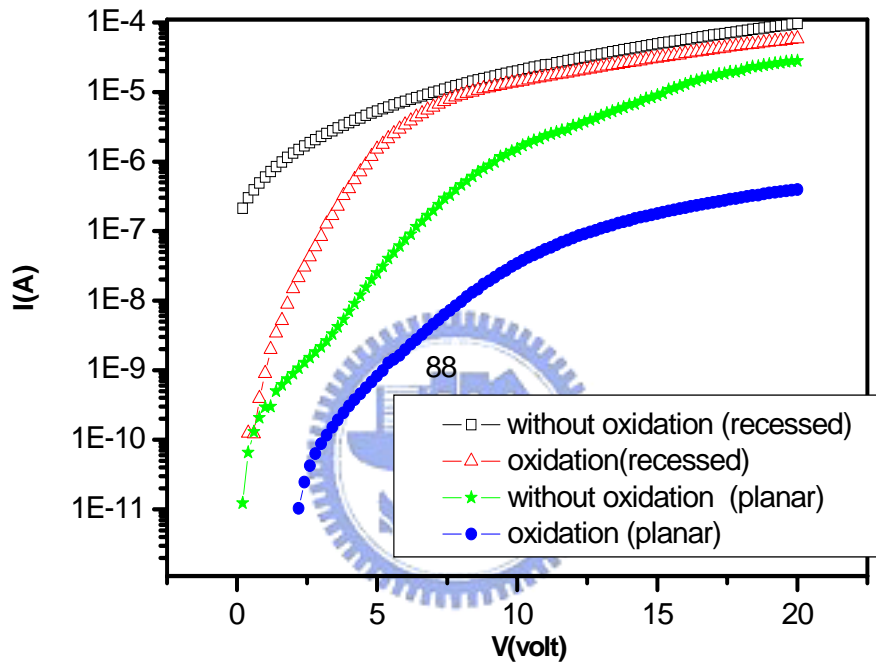


Fig.4.3 The dark I-V characteristics of the planar and recessed-electrode GaN MSM-PDs with or without oxidation. (For example, PD with 3 μm spacing and 8 μm wide metal finger is denoted as 38.)

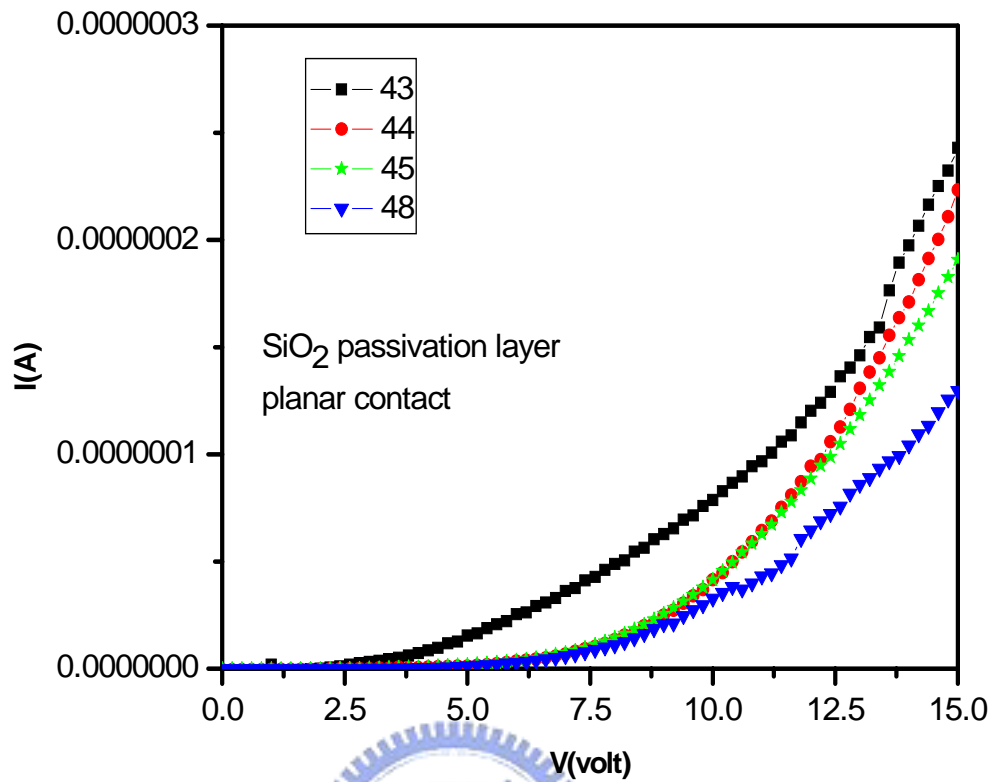


Fig.4.4 Dark current versus bias voltage for various the planar Pt GaN MSM-PDs with finger width =3, 4, 5, 8 μ m and the same finger space = 4 μ m.

For the different geometry figures, we have measured the dark current versus bias voltage. From Fig.4.2 and Fig.4.4, we discuss further the dark current of the planar MSM-PDs.

- (1) The internal leakage current, I_{in} , flows through the depletion regions and semiconductors from the reverse-bias contacts to the forward-bias contacts. The leakage increases with the finger density and the finger width of MSM PDs,

$$I_{in} \propto \frac{W}{S + W} \dots\dots\dots (4.1)$$

For the finger width 3μm, the ratio from Equation (4.1) is $\frac{3}{7}$, and 8μm, the ratio from Equation (4.1) is $\frac{8}{12}$, with the finger spacing width 4μm, the dark current of the former should be lower than the latter. Fig 4.4 shows the opposite trend. The internal leakage current is not the main control in the conventional MSM PDs.

(2) Surface leakage current flows on the surface of GaN. It increases with the finger density of MSM PDs and decreases with the finger spacing width.

$$I_s \propto \frac{1}{(S + W) \times S} \dots\dots\dots (4.2)$$

For the finger width 4μm, the ratio from Equation (4.2) is $\frac{1}{32}$, and 8μm, the ratio from Equation (4.2) is $\frac{1}{48}$, with the finger space width 4μm, the dark current of the former should be near 1.5 times higher than the latter. In Fig 4.4, these two MSM PDs shows the same tend. Under 15V bias, the dark current of the device with finger spacing width 4μm and the finger width 4μm is near 0.22μA and the dark current of the device with finger spacing width 4μm and the finger width 8μm is near 0.13μA. The surface leakage current controls the dark current of planar GaN MSM PDs mainly. On the other hand, the dark current of the recessed electrode MSM-PDs is also shown in Fig.4.5.

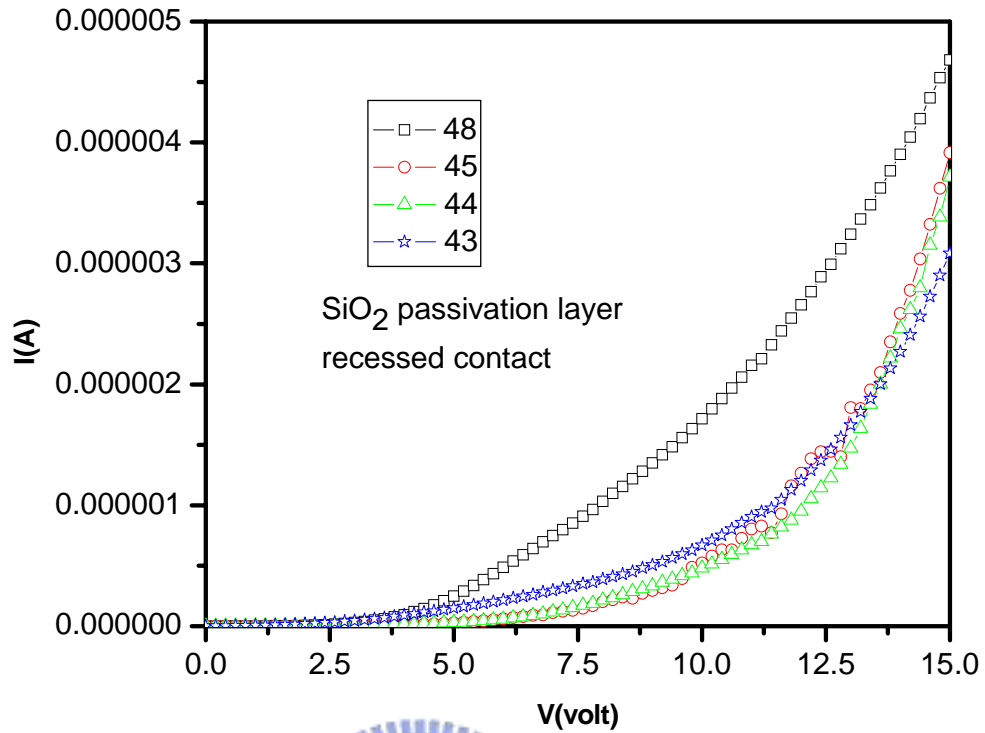
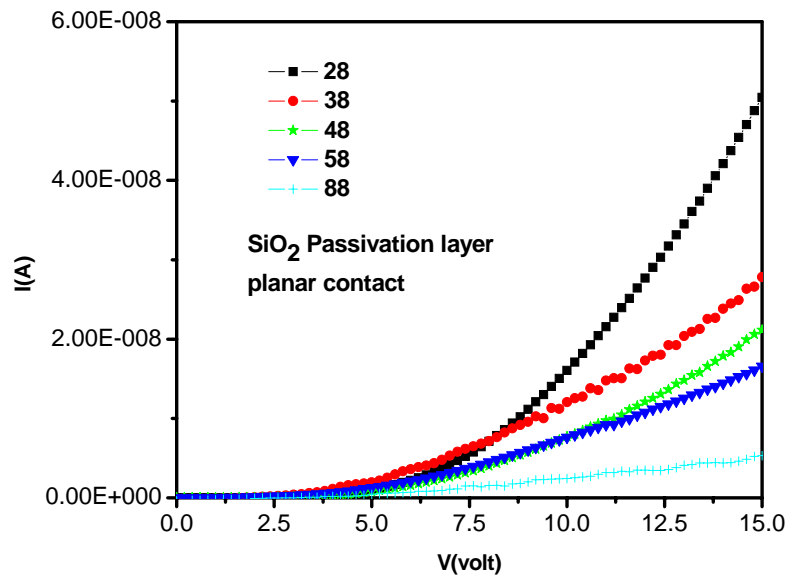
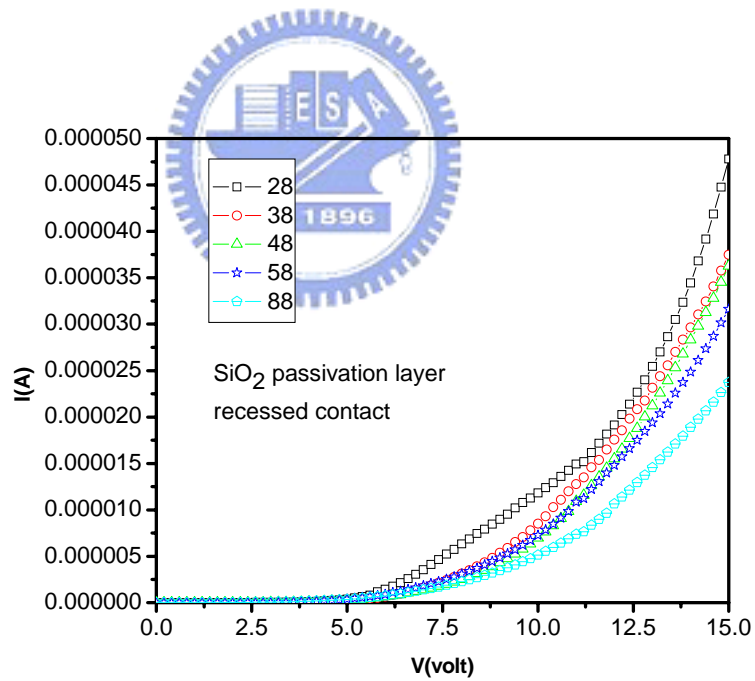


Fig.4.5 Dark current versus bias voltage for various the recessed Pt/GaN MSM-PDs with finger width =3, 4, 5, 8 μm and the same finger space = 4 μm .

For the finger width 3 μm , the ratio from Equation (4.1) is $\frac{3}{7}$, and 8 μm , the ratio from Equation (4.1) is $\frac{8}{12}$, with the finger spacing width 4 μm , the dark current of the former should be lower than the latter. Fig 4.5 shows the same trend. The internal leakage current is the main control in the recessed MSM PDs. Under 15V bias, the dark current of the device with finger spacing width 4 μm and the finger width 4 μm is near 3.7 μA and the dark current of the device with finger spacing width 4 μm and the finger width 8 μm is near 4.7 μA . The internal leakage current controls the dark current of recessed GaN MSM PDs mainly.



(a) The planar MSM PDs



(b) The recessed-electrode MSM PDs

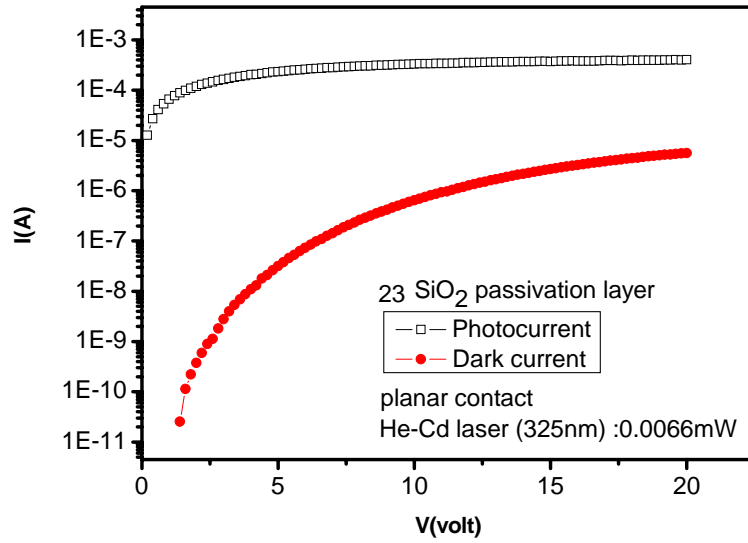
Fig.4.6 The I-V characteristics of (a) the planar and (b) recessed-electrode the MSM PDs with finger space width = 2, 3, 4, 5, 8 μm and the same finger width = 8 μm .

For the finger width $4\mu\text{m}$, the ratio from Equation (4.2) is $\frac{1}{32}$, and $8\mu\text{m}$, the ratio from Equation (4.2) is $\frac{1}{48}$, with the finger space width $4\mu\text{m}$, the dark current of the former should be near 1.5 times higher than the latter. In Fig 4.5, these two MSM PDs shows the opposite tend.

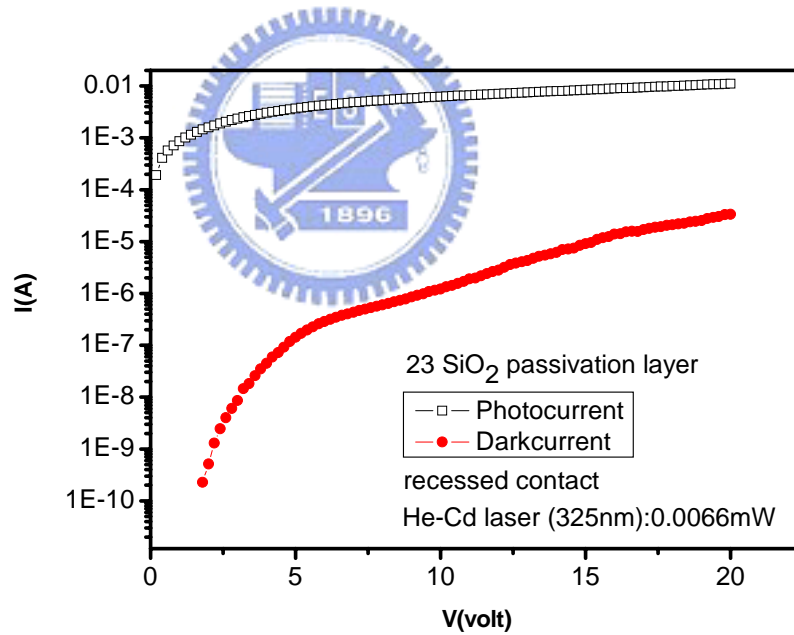
Fig.4.6 shows the I-V characteristics of (a) the planar and (b) recessed electrode the MSM PDs with finger space width =2, 3, 4, 5, $8\mu\text{m}$ and the same finger width = $8\mu\text{m}$. From Fig.4.6 (a), we can find that the surface leakage current dominates the dark current in the planar MSM PDs. Furthermore, Fig.4.6 (b) shows the internal leakage current is the important part of the dark current in the recessed electrode MSM PDs.

4.3 Photo current of GaN MSM photo detector

Fig 4.7 illustrates the photo and dark current of (a) planar and (b) recessed electrode MSM PDs with finger spacing width $2\mu\text{m}$ and finger width $3\mu\text{m}$ versus applied bias under illumination (He-Cd laser :0.0066mW). In the planar MSM PDs, the photo current is $4.0071\text{E-}4$ A when applied voltage is 20V and the ratio of photo to dark current is 71 ($I_{\text{dark}}=5.6343\text{E-}6\text{A}$). In the recessed electrode MSM PDs, the photo current is 0.01104 A when applied voltage is 20V and the ratio of photo to dark current is 326 ($I_{\text{dark}}=3.3787\text{E-}5\text{A}$). From Fig.4.7, it was found that photocurrent to dark current contrast ratios were 326 and 70 for the MSM-PDs with and without recessed electrodes under a 20V applied bias, respectively.



(a) planar MSM PD



(b) Recessed-electrode MSM PD

Fig 4.7 The photo and dark current of (a) planar and (b) recessed-electrode MSM PDs with finger spacing width $2\mu\text{m}$ and finger width $3\mu\text{m}$ versus applied bias under illumination (He-Cd laser :0.0066mW).

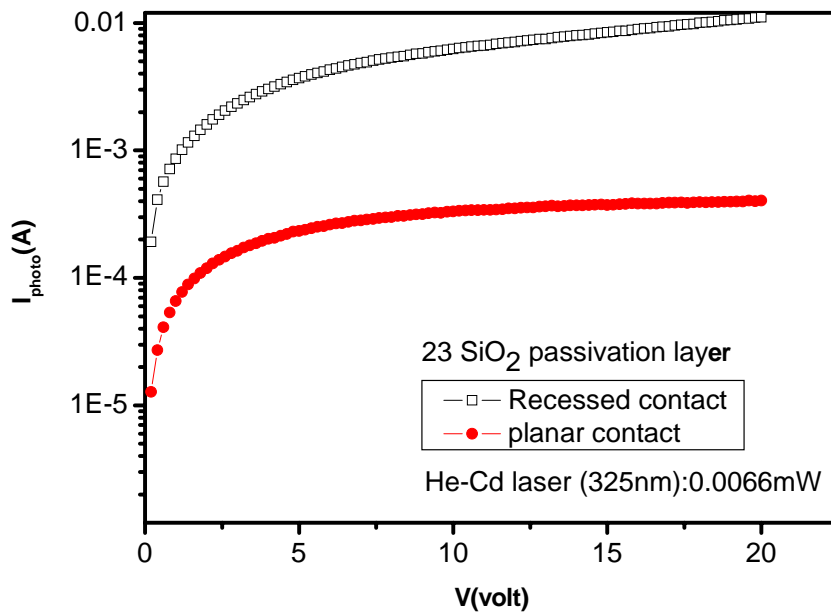


Fig. 4.8 The I-V characteristics of the planar and recessed-electrode GaN MSM PDs under illumination (He-Cd laser :0.0066mW).

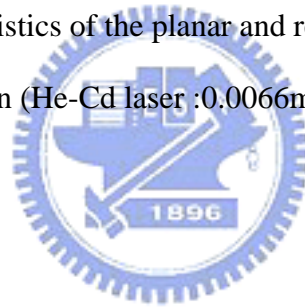


Fig.4.8 shows the I-V characteristics of the planar and recessed-electrode GaN MSM PDs under illumination (He-Cd laser :0.0066mW). We found that photocurrent observed from the MSM-PD with recessed electrodes was larger than that of planar MSM-PD by about one order of magnitude. From Fig 4.7 and 4.8, we believe these observations should be related to the enhanced electric field or the uniform electric field distributed through the gap space in the recessed electrode structure.

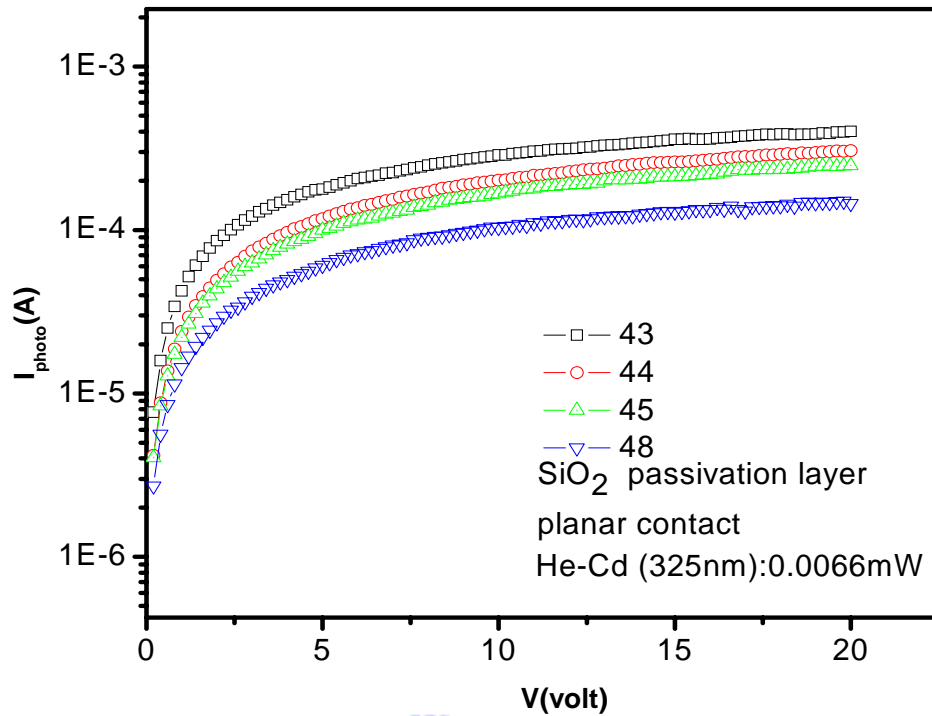


Fig 4.9 Photo current of the planar MSM PDs with the finger space width $s = 4\mu\text{m}$ and different finger width $w = 3, 4, 5, 8\mu\text{m}$ versus applied bias.

For the different finger width, we also measure their photo current. As the thickness of our metal is 100 \AA that is like transparent metal, most of the depletion region under the finger metal can also absorb the photon to generate the photo current. The total area of finger region plays the more important role than the space region because of the transparent metal. In Fig.4.9, the photo current of the conventional MSM PDs with the finger space width $s = 4\mu\text{m}$ and different finger width $w = 3, 4, 5, 8\mu\text{m}$ versus applied bias are shown. The wide finger width the lower photo response can be seen in Fig.4.9.

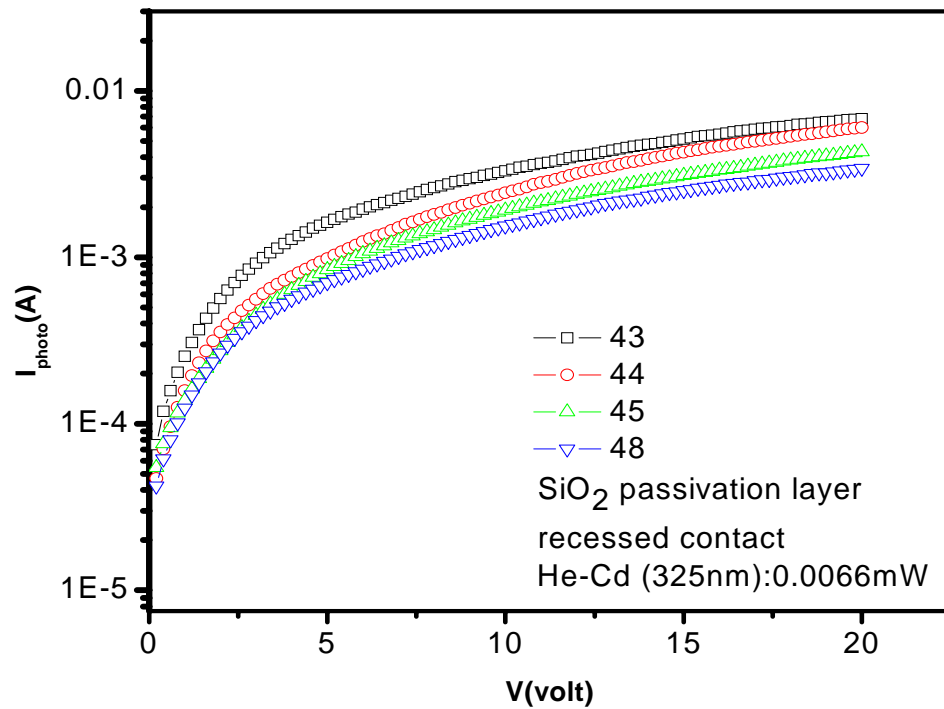


Fig 4.10 Photo current of the recessed-electrode MSM PDs with the finger space width $s = 4\mu\text{m}$ and different finger width $w = 3, 4, 5, 8\mu\text{m}$ versus applied bias.

Fig. 4.10 shows the photo current of the recessed-electrode MSM PDs with the finger space width $s = 4\mu\text{m}$ and different finger width $w = 3, 4, 5, 8\mu\text{m}$ versus applied bias. The wide finger width the lower photo response can be also seen in Fig.4.10. In other words, more photo current can be induced when raises the density of finger metal.

4.4 Photo response of GaN MSM photo detector

The optical spectrum measurement setups of MSM PDs are shown in Fig 3.9. Fig. 4.11 illustrates the normalized responsivity of the planar MSM PD with Pt metals under a 2V applied bias. An abrupt exponential cut-off wavelength of 365nm demonstrates the structure impressive wavelength selective below and above the gap.

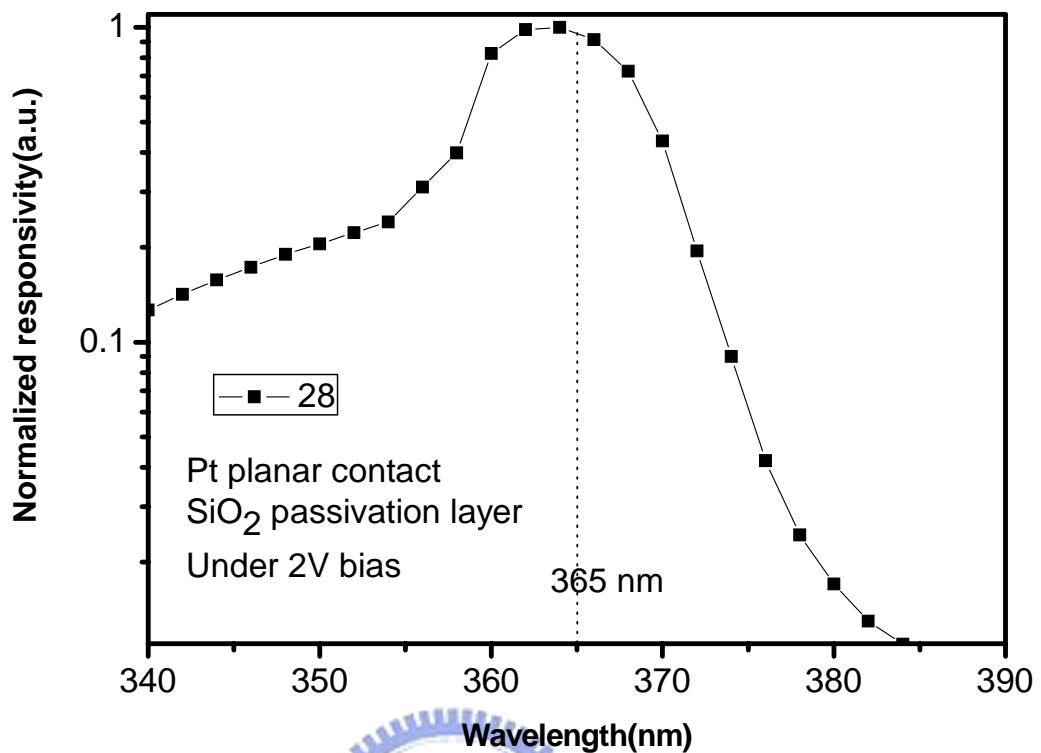


Fig. 4.11 The normalized responsivity of the planar MSM PD with Pt metals under a 2V applied bias.

The response in the UV is almost three orders of magnitude greater than visible region (500 nm) of the spectrum, which compares favorably well with the other reported results, indicating a good spectral selectivity and high quantum efficiency up to cut-off wavelength. The spectral selectivity and below band gap response (>365 nm) are important for UV application, which we believe may be associated with deep-level defect states, its magnitude is an indication of the density of defects in the GaN. Because the GaN has a wide band gap, crystal defects or impurities in the material may easily create energy levels within the gap. These levels form recombination centers that harm the performance of UV photodetectors, in

particular their visible blindness. Better control of the material growth technology (reduction of impurities and defect densities) is needed to improve the visible blindness for our GaN-based UV detectors.

Fig. 4.12 and Fig 4.13 show the responsivity of the planar and recessed-electrode MSM PDs with the finger space width $s = 2\mu\text{m}$ and different finger width $w = 3, 4, 5, 8\mu\text{m}$ under a 2V applied bias. The wide finger width the lower responsivity can be seen in Fig.4.12 and Fig.4.13. This trend is matched with Fig. 4.9 and Fig. 4.10. The responsivity of MSM PDs increases when raises the density of the finger metal. The response range of these detectors is from 310 to 370nm.

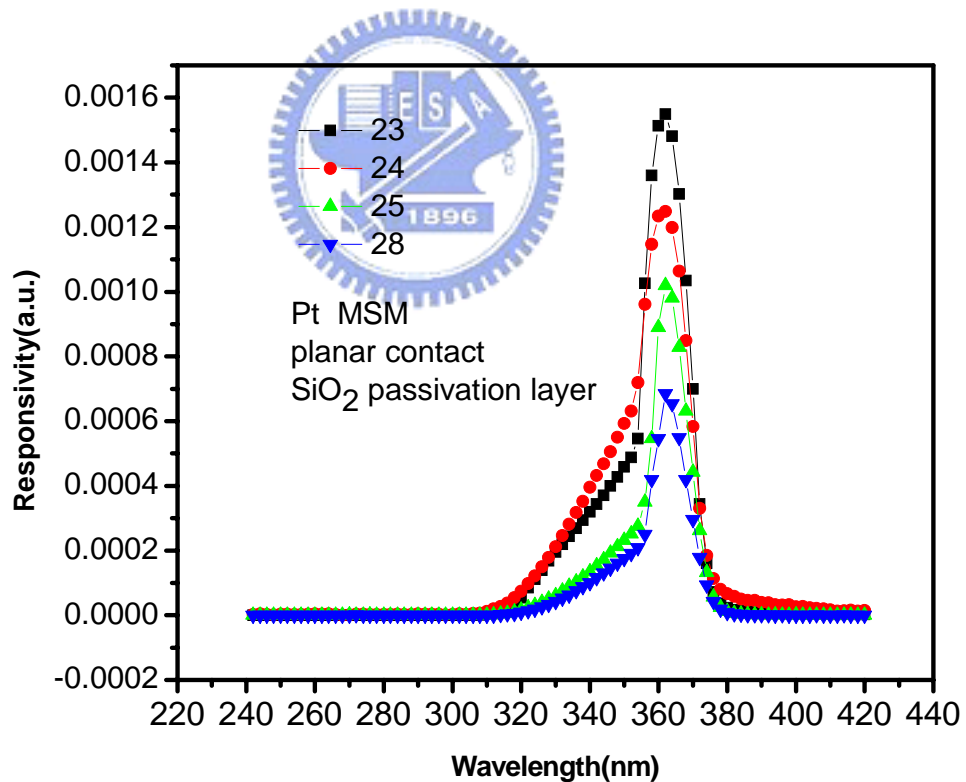


Fig 4.12 The responsivity of the planar MSM PDs with the finger space width $s = 2\mu\text{m}$ and different finger width $w = 3, 4, 5, 8\mu\text{m}$ under 2V bias.

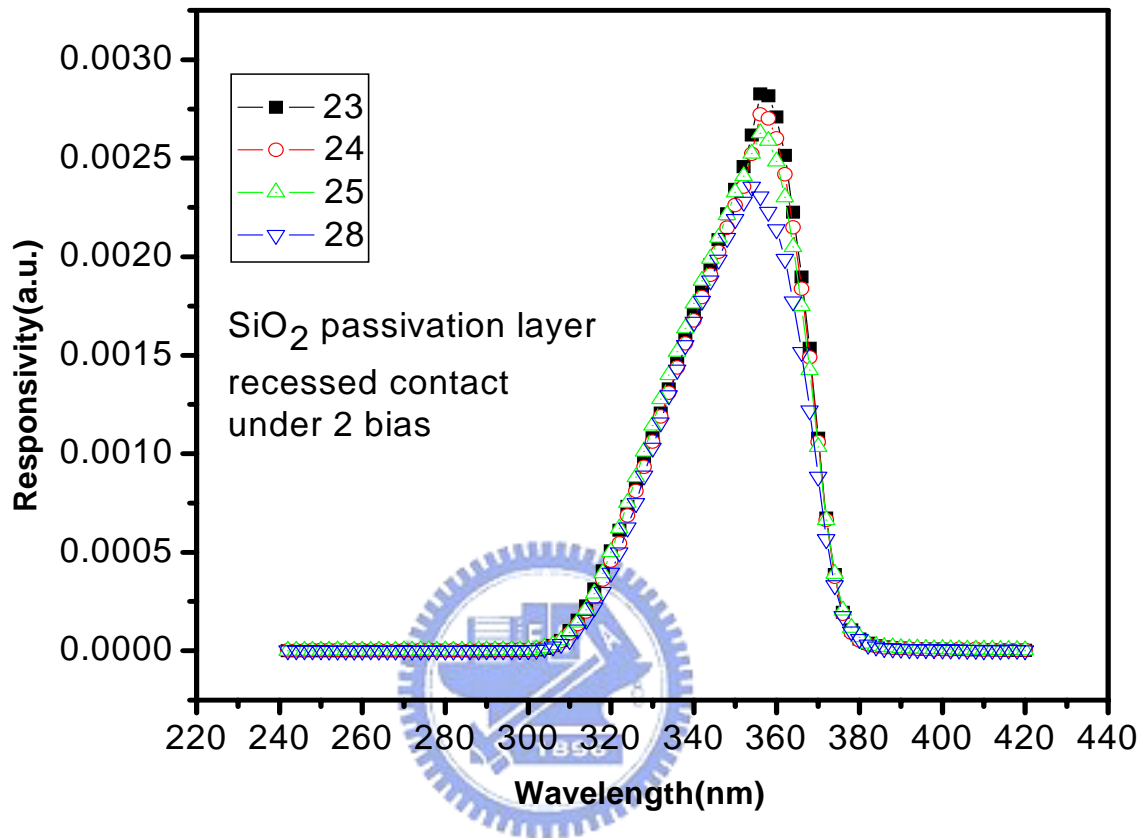


Fig 4.13 The responsivity of recessed-electrode MSM PDs with the finger space width $s = 2\mu\text{m}$ and different finger width $w = 3, 4, 5, 8\mu\text{m}$ under 2V bias.

To get the relative responsivity of MSM PDs, we divided the original spectral response of MSM PD to that of a PMT under the same measurement condition and multiplied the responsivity of the PMT device. The monochromatic light is calibrated with PMT and an optical power meter. Fig. 4.14 shows spectral responses of the recessed-electrode and the planar MSM PDs with a 2V applied bias. With a 2V applied bias and an incident light wavelength of 360 nm, it was found that measured responsivities were 0.019 and 0.0094A/W for the MSM-PDs with and without recessed electrodes, respectively.

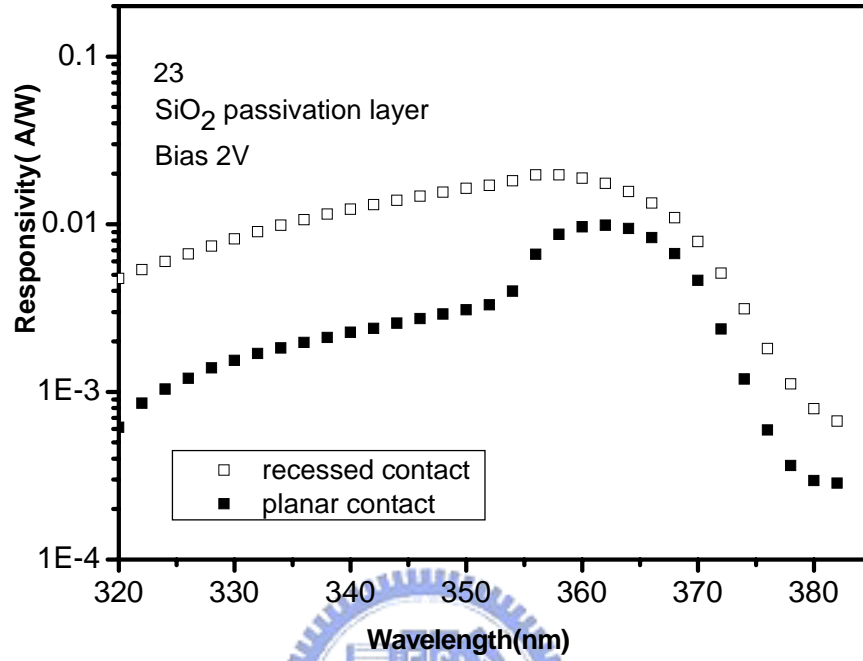



Fig. 4.14 The spectral responses of the recessed-electrode and the planar MSM PDs with a 2V applied bias.

Chapter 5

Conclusion

In this study, we fabricated and characterized the interdigitated metal-semiconductor-metal (MSM) photodetectors (PDs) onto the undoped GaN substrates. Pt was used for the metal electrodes in our MSM PDs. Various geometric structures of metal electrodes and semiconductor surface passivation MSM detectors and surface were invoked to investigate dark current sources in the MSM PDs. To our experimental results, for the same passivation layer over semiconductor surface, the dark current is mainly resulted from the surface leakage current for planar-electrode MSM detectors and is dominant by the internal leakage current for recessed-electrode MSM detectors.



The fabricated MSM PDs work well for UV-light detection. The photosensitive spectrum range is between 310 and 370 nm for our MSM PDs. It was found that photocurrent and the contrast ratio of photocurrent to dark current ratio of recessed-electrode MSM PDs are both larger than those of planar electrode MSM PDs under the same bias voltage and illumination intensity. For example, the contrast ratio is 326 for a recessed-electrode MSM PD and is 70 for a planar-electrode MSM PD under a bias voltage of 20 V and the light intensity of $0.0115\text{W}/\text{cm}^2$. The peak responsivity of the planar-electrode MSM detectors is $0.009\text{ A}/\text{W}$ at 360 nm, while the peak responsivity of the recessed-electrode MSM detectors is $0.019\text{ A}/\text{W}$ at 360nm.

Reference

1. Donati, Silvano, Photodetectors : devices, circuits, and applications, Upper Saddle River, NJ :Prentice Hall PTR, c2000.
2. Hari Singh Nalwa, Photodetectors and fiber optics, San Diego, CA: Academic Press, c2001.London.
3. S. D. Lester, M. J. Ludowise, Killeen, B. H. Perez, J. N. Miller, and S. J. Rosner, J. Cryst. Growth, vol. 189, p.786, 1998.
4. A. osinsky, S. Gangopadhyay, J. W. Yang, R. Gaska, D.V. Kuksenkov, H. Temkin, I. K. Shmagin, Y. C. Chang, J. F. Muth, and R. M. Kolbos, Appl. Phys. Lett. 72, 551(1998).
5. L. Wang, M. I. Nathan, T-H. Lim, M. A. Khan, and Q. Chen, Appl. Phys. Lett. 68, 1267(1996).
6. L. Leung, A. F. Wright, and E. B. Stechel, Appl. Phys. Lett. 74, 2495(1999).

V. Mikhelashvili, G. Eisenstein, V. Graber, S. Fainleib, G. Bahir, D. Ritter, M. Orenstein, and A. Peer, J. Appl. Phys. 85, 6873(1999).
7. S. Strite and H. Morkoc, J. Vac. Sci. Technol. B 10, 1237(1992)
8. J. C. Carrano, T. Li, P. A. Grudowski, C. J. Eiting, R. D. Dupuis, and J. C. Campbell, J. Appl. Phys. 83, 6148(1998).
9. E. Monroy, F. Calle, E. Munoz, F. Omnes, Phys. Status Solidi A 176, 141(1999).

10. J. C. Carrano, T. Li, P. A. Grudowski, C. J. Eiting, R. D. Dupuis, and J. C. Campbell, *J. Appl. Phys.* 70, 1992(1997).
11. V Adivarahan, G. Simin, J. W. Yang, A. Lunev, M. AsifKhan, N. Pala, M. Shur, and R. Gaska, *Appl. Phys. Lett.* 77, 863(2000)
12. Donald A. Neamen, *Semiconductor Physics & Devices*, third Edition.
13. S.M. Sze, *Physics of semiconductor devices*. New York: John Wiley & Sons 1981.
14. S.M. Sze, D. J.Coleman, JR. and A. Loya, *Solid-State Electronics* 14(1971), p1209-1218.
15. F. A. Padovani, R. Stration, *Solid-State Electronics* 9(1966), p695-707.
16. Schubert F. Soares, *Jap. J. Appl. Phys.*31(1992), p210-216.
17. M. Klingenstein, J. Kuhi, J Rosenzweig and etc, *Solid-State Electronics* 2(1994), p333-340.
18. O. Katz, V. Garber, B. Meyler and etc, *Appl. Phys. Lett.* 79(2001), p1417-1419.
19. Rough-Heng Yuang and Jen-Inn Chyi, *IEEE Journal of quantum electronics*, 34(1998), p811.
20. 陳姿均，「氮化鎵金屬-半導體-金屬光偵測器之製程與光電特性」，國立交通大學，碩士論文，民國 92 年。